Biogeosciences

Discussions

Open Access

EGU

Benthic alkalinity and DIC fluxes in the Rhône River prodelta

generated by decoupled aerobic and anaerobic processes

Jens Rassmann[a,1] , Eryn M. Eitel[b, 1], Cécile Cathalot[c], Christophe Brandily[c],
Bruno Lansard[a] , Martial Taillefert[b] , Christophe Rabouille[a, 2]

[a] *Laboratoire des Sciences du Climat et de l'Environnement, LSCE/IPSL,CEA-CNRS-UVSQ-Université Paris Saclay, 91198 Gif-sur-Yvette, France*

[b] *School of Earth and Atmospheric Sciences; Georgia Institute of Technology, GA 30332-0340 Atlanta, USA*

[c] *IFREMER, Laboratoire Environnement Profond, 29280 Plouzané, France*

[1]Jens Rassmann and Eryn M. Eitel contributed equally to this article
[2] Corresponding author
    Email adress: rabouill@lsce.ipsl.fr (Christophe Rabouille)
    ORCID: https://orcid.org/0000-0003-1211-717X

1

Biogeosciences
Discussions

Abstract

2   Estuarine regions are generally considered a net source of atmospheric CO_2 as a result of the high

3 organic carbon (OC) mineralization rates in the water column and their sediments. Yet, the intensity

4 of anaerobic respiration processes in the sediments tempered by the reoxidation of reduced

5 metabolites controls the net production of alkalinity from sediments that may partially buffer the

6 metabolic CO_2 generated by OC respiration. In this study, a benthic chamber was deployed in the

7 Rhône River prodelta and the adjacent continental shelf (Gulf of Lions, NW Mediterranean) to assess

8 the fluxes of total alkalinity (TA) and dissolved inorganic carbon (DIC) from the sediment.

9 Concurrently, *in situ* O_2 and pH microprofiles, electrochemical profiles, pore water and solid

10 composition were measured in surface sediments to identify the main biogeochemical processes

11 controlling the net production of alkalinity in these sediments. The benthic fluxes of TA and DIC,

12 ranging between 14 and 74 mmol m^{-2} d^{-1} and 18 and 78 mmol m^{-2} d^{-1}, respectively, were up to 8 times

13 higher than the DOU fluxes (10.4 ± 0.9 mmol m^{-2} d^{-1}) close to the river mouth, but their intensity

14 decreased offshore, as a result of the decline in OC inputs. Low nitrate concentrations and strong pore

15 water sulfate gradients indicated that the majority of the TA and DIC was produced by sulfate and

16 iron reduction. Despite the complete removal of sulfate from the pore waters, dissolved sulfide

17 concentrations were low due to the precipitation and burial of iron sulfide minerals (12.5 mmol m^{-2}

18 d^{-1} near the river mouth), while soluble organic-Fe(III) complexes were concurrently found

19 throughout the sediment column. The presence of organic-Fe(III) complexes together with low sulfide

20 concentrations and high sulfate consumption suggests a dynamic system driven by the variability of

21 the organic and inorganic particulate input originating from the river. By preventing reduced

22 substances from being reoxidized, the precipitation and burial of iron sulfide decouples the iron and

23 sulfur cycles from oxygen, therefore allowing a flux of alkalinity out of the sediments. In these

24 conditions, the sediment provides a source of alkalinity to the bottom waters which mitigates the

25 effect of the benthic DIC flux on the carbonate chemistry of coastal waters.

Keywords

26 Carbon cycle; alkalinity flux; iron reduction; sulfate reduction; coupled element cycles

27 **1. Introduction**

28   As a link between continental and marine environments, the coastal ocean plays a key role in the

29 global carbon cycle (Bauer et al., 2013). In particular, large fluxes of dissolved and particulate organic

30 carbon (POC) are delivered by rivers to neighbouring continental shelves (Bianchi and Allison, 2009).

31 In fact, even though shelf regions only occupy around 7 % of the global ocean surface area (Jahnke,

32 2010), they account for more than 40 % of POC burial in the oceans of which about half is buried in

33 river deltas and estuaries (Hedges and Keil, 1995; McKee et al., 2004; Muller-Karger et al., 2005;

34 Chen and Borges, 2009). River-dominated ocean margins receive substantial amounts of

35 allochthonous and authigenic POC that settle to the sea floor (Rabouille et al., 2001; Burdige, 2005;

36 Andersson et al., 2006), therefore increasing the organic carbon content of the sediments and

37 enhancing mineralization rates (Canfield et al., 1993a; Mckee et al., 2004; Muller-Karger et al., 2005;

38 Aller et al., 2008; Burdige, 2011). These processes allow estuarine and deltaic regions to constitute a

39 net source of CO_2 to the atmosphere (Chen and Borges, 2009, Cai, 2011). In these river-dominated

40 margins, high sedimentation rates of material containing large concentrations of POC decrease the

41 residence time of organic carbon in the oxic sediment layers (Hartnett et al., 1998) and increase the

42 relative contribution of anaerobic compared to aerobic degradation pathways of organic carbon

43 (Canfield et al., 1993a). Anaerobic respiration processes, including denitrification, dissimilatory

44 nitrate reduction to ammonium (DNRA), manganese reduction, iron reduction, and sulfate reduction

45 create total alkalinity (TA) (Berner, 1970; Dickson, 1981; Wolf-Gladrow et al., 2007, Table 1) that

46 increases the buffer capacity of pore waters (Ben-Yaakov, 1973; Soetaert et al., 2007), drives the

47 carbonate saturation state of the pore waters towards oversaturation, and potentially trigger carbonate

48 precipitation (Gaillard et al., 1989; Mucci et al., 2000; Jørgensen and Kasten, 2006; Soetaert et al.,

49 2007; Burdige, 2011). In turn, the precipitation of carbonate species, such as calcite and aragonite,

50 consumes alkalinity within the sediments (Table 1, Eq. 1; Berner, 1970; Soetaert et al., 2007; Krumins

51 et al., 2013; Brenner et al., 2016). Anaerobically produced alkalinity may also be consumed close to

52 the sediment-water interface (SWI) by the aerobic reoxidation of reduced species such as NH_4^+, Mn^{2+},

53 Fe^{2+}, and dissolved sulfide (Table 1, Eq. 2-4; Jourabchi et al., 2005; Krumins et al., 2013; Brenner et

54 al., 2016). However, the precipitation and ultimate burial of iron sulfide minerals may prevent

55 reoxidation of dissolved sulfide and Fe^{2+} and result in the net production of alkalinity in sediments.

56 Thus, the net TA flux across the SWI depends on the type and intensity of anaerobic respiration, on

57 carbonate precipitation/dissolution and whether reduced species are reoxidized by dissolved oxygen

58 after diffusion upwards or trapped in anaerobic sediment layers by precipitation (Hu and Cai, 2011a;

59 Krumins et al., 2013; Łukawska-Matuszewska et al., 2018).

60   To characterize the biogeochemical conditions in which sediments provide an alkalinity source

61 to coastal waters, it is crucial to relate this reaction network to net benthic fluxes of alkalinity and

62 dissolved inorganic carbon (DIC) measured *in situ*. A high ratio (> 1) of benthic TA to DIC fluxes

63 would increase the buffer capacity of the bottom waters. This could influence the coastal carbon cycle

64 by increasing the storage capacity of CO_2 in coastal waters over long time scales (Thomas et al., 2009;

65 Andersson et al., 2012; Brenner et al., 2016). The objectives of this study were to investigate if

66 sediments from deltaic regions exposed to large riverine inputs of carbon and minerals represent an

67 alkalinity source to the bottom waters and identify the biogeochemical processes responsible for the

68 net production of alkalinity in these sediments. To achieve these objectives, TA and DIC benthic

69 fluxes, dissolved oxygen uptake (DOU) fluxes, burial fluxes of reduced substances and the main

70 biogeochemical processes involved in organic carbon mineralization in sediments were determined

71 along a gradient of organic carbon and mineral inputs to the sea floor in the Rhône River delta

72 (France).

Biogeosciences
Discussions

Open Access

EGU

73 **2. Study site and methods**

74 *2.1 The Rhône River delta*

75   The Rhône River subaqueous delta, also called prodelta due to its prograding characteristics, is

76 a wave-dominated delta located in the Gulf of Lions (France), a microtidal continental margin. The

77 Rhône River is the main source of freshwater, sediments (including iron oxides), and POC to the

78 Mediterranean Sea (Sempéré et al., 2000). The river plume is generally oriented southwestward due

79 to the combined effects of wind forcing and the Coriolis effect (Estournel et al., 1997). The Grand

80 Rhône River mouth is characterized by a prodeltaic lobe (Got et al., 1990) that can be divided into

81 three main areas based on bathymetry and sedimentation rates: the proximal domain within a 2 km

82 radius of the river outlet and with water depths between 10 and 30 m; the prodelta domain between 2

83 and 5 km with water depths ranging from 30 to 70 m; and the distal domain further offshore with

84 water depths greater than 70 m. The sediments of the three domains are characterized by a strong

85 biogeochemical gradient from the Rhône River mouth to the Gulf of Lions continental slope (Lansard

86 et al., 2009).

87   Most of the riverine particles settle in the vicinity of the river mouth leading to mean apparent

88 accumulation rates of up to 37-48 cm yr^{-1} (Charmasson et al., 1988), including about 80 % of the

89 particles deposited during flood events (Maillet et al., 2006; Cathalot et al., 2010). Thus, sediments

90 from the proximal domain are dominated by the periodic accumulation of terrestrial organic-rich

91 particles (Radakovich et al., 1999; Roussiez et al., 2005). Offshore, sedimentation rates decrease

92 rapidly and reach typical values for shelf regions (< 0.1 cm yr^{-1}), in the distal domain (Miralles et al.,

93 2005). The sediments in all the study area are fine grained and of cohesive nature (Roussiez et al.,

94 2005). Their total organic carbon content is higher than 2 % close to the river mouth and decreases

95 offshore (Lansard et al., 2008). The sedimentary inorganic carbon content ranges between 28 and

96 38 % (Roussiez et al., 2005) and is mostly composed of calcite and magnesian calcite (Rassmann et

97 al., 2016). Sediment respiration rates are high in the proximal domain and decrease offshore (Lansard

98 et al., 2009; Pastor et al., 2011; Cathalot et al., 2013; Rassmann et al., 2016). These sediments are

99 characterized by strong anaerobic production of TA and DIC (Rassmann et al., 2016), but whether

100 this alkalinity is consumed in the oxic sediment layer or released to the bottom waters has yet to be

101 determined.

102 *2.2 Bottom water sampling and analyses*

103   The AMOR-B-Flux cruise took place on-board the RV Tethys II (CNRS-INSU) in September

104 2015. The investigated stations were located in the river plume along a nearshore-offshore transect

105 (Fig. 1 and Table 2). Bottom water samples were collected with 12-L Niskin® bottles as close as

106 possible to the sea floor. The seawater temperature was measured using a thermometer with a

107 precision of 0.1 °C and the salinity with a conductivity based thermosalinometer with a precision of

108 0.1. Triplicate pH measurements, reported on the total proton scale (pH_T), were carried out within 1

109 hour after sampling by spectrophotometry with unpurified m-cresol purple as indicator dye (Clayton

110 and Byrne, 1993) and a precision of ± 0.01 pH units. Dissolved oxygen concentrations were analysed

111 by Winkler titration (Grasshoff et al., 1983) within twelve hours after sampling with a precision of ±

112 0.5 μM.

113 *2.3 In situ benthic chamber deployments*

114   Benthic fluxes and sediment depth profiles of the main redox species involved in the

115 remineralization of organic carbon were determined with an autonomous benthic lander (Jahnke et

116 and Christiansen, 1989). The lander was equipped with a single benthic chamber, water syringe

117 sampling system, and retrofitted with a programmable, battery-powered ISEA IV In Situ

118 Electrochemical Analyzer and a SUBMAN-1 in situ micromanipulator from Analytical Instrument

119 Systems, Inc. (AIS, Inc.) to simultaneously obtain depth profiles of redox chemical species with

120 mercury/gold (Hg/Au) amalgam voltammetric microelectrodes (Luther et al., 2008; Tercier-Waeber

121 and Taillefert, 2008). The chamber encloses a 30 x 30 cm sediment surface area with a certain volume

122 of overlying water determined by measuring the concentration of two tracers (iodide and bromide)

123 injected immediately after closure of the chamber. Homogenization of the overlying waters was

124 assured with a stirrer integrated in the chamber lid. TA and DIC concentrations were determined in

125 the benthic chamber water samples collected as a function of time. The slopes of the concentration-

126 time plots were estimated using a restricted maximum likelihood estimator (REML) that takes

127 uncertainties of individual measurements into account. Finally, benthic fluxes across the SWI (F_i)

128 were calculated from the slopes of these concentration-time-plots and the chamber height (Eq. 1),

$$F_i = H \cdot \frac{dC_i}{dt} \tag{1}$$

129 where H is the overlying water height in the benthic chamber, C_i represents the concentration of the

130 analyte i (TA or DIC), and t is time.

131 *2.4 In situ microprofiling of dissolved oxygen and pH*

132   A separate benthic lander, carrying a benthic microprofiler (Unisense®), was deployed to measure

133 *in situ* microprofiles of dissolved oxygen and pH (Cai and Reimers, 1993; Rabouille et al., 2003,

134 Rassmann et al., 2016 and references therein). Up to five oxygen and two pH microelectrodes were

135 simultaneously deployed, and vertical depth profiles were measured with a 200 μm resolution. As

136 their response to variations in oxygen concentrations is linear, the O_2 microelectrodes were calibrated

137 with a two-point calibration technique using the bottom water O_2 concentration determined by

138 Winkler titration and the anoxic pore waters. The pH microelectrodes were calibrated using NBS

139 buffers (pH 4.00, 7.00 and 9.00 at 20°C) and the spectrophotometrically determined pH of the bottom

140 waters was used to correct for the difference in the liquid junction potential between seawater and the

141 NBS buffers. Signal drift of O_2 and pH microelectrodes during profiling was checked to be less than

142 5 %.

143 *2.5 Sediment sampling, porosity measurements, and ex situ voltammetric profiling*

144   At each sampling station, sediment cores were collected using an UWITEC® single corer (length

145 60 cm, inner diameter 9 cm) within 30 m from the site where the landers were deployed and processed

146 within 30 minutes after collection. Sediment porosity profiles were determined by slicing one of the

147 cores with a 2 mm resolution until 10 mm depth, a 5 mm resolution until 60 mm, and a 10 mm

148 resolution down to the bottom of the cores. Porosity was calculated from the bottom water salinity,

149 an average sediment density of 2.65 g cm^{-3} and the weight difference between the wet and dried

150 sediment after one week at 60 °C.

151   *Ex situ* voltammetric profiles were obtained in a separate core with a AIS, Inc. DLK-70

152 potentiostat in a three electrode configuration, including Hg/Au working microelectrode constructed

153 from Pyrex glass pulled to a tip of 0.4 mm diameter to minimize particle entrainment during the

154 profiles (Luther et al., 2008), an Ag/AgCl reference electrode, and a platinum counter electrode. The

155 Hg/Au voltammetric electrode was deployed in the sediment using a DLK MAN-1 micromanipulator

156 (AIS, Inc). Using a combination of linear sweep and anodic and cathodic square wave voltammetry,

157 Hg/Au voltammetric microelectrodes are able to simultaneous quantify dissolved O_2, Mn^{2+}, Fe^{2+},

158 total dissolved sulfide ($\Sigma H_2S = H_2S + HS^- + S^0 + S_x^{2-}$), as well as organic complexes of Fe(III) (org-

159 Fe(III)) and iron sulfide clusters (FeS_{aq}), which are not quantifiable but reported in normalized current

160 intensities (Tercier-Waeber and Taillefert, 2008). Hg/Au microelectrodes were calibrated for

161 dissolved O_2 using *in situ* temperature and salinity of the overlying waters to determine the dissolved

162 O_2 concentrations at saturation (Luther et al., 2008). They were also calibrated externally with $MnCl_2$

163 to quantify all other species according to the pilot ion method (Luther et al., 2008). All voltammetric

164 data was integrated using VOLTINT, a semiautomated Matlab® script with peak recognition software

165 (Bristow and Taillefert, 2008).

2.6 Pore water and solid phase extractions and analyses

166

167   Sediment pore waters were extracted using rhizon filters with a mean pore size of 0.1 μm

168 (Seeberg-Elverfeldt et al., 2005) in a glove bag that was extensively flushed with N_2 to create an

169 anaerobic atmosphere. Pore waters were analyzed immediately onboard for dissolved phosphate

170 concentrations using the paramolybdate method (Murphy and Riley, 1962) as well as for dissolved

171 Fe^{2+} and total dissolved iron concentrations using the ferrozine method (Stookey, 1970). Pore water

172 and bottom water fractions were poisoned with $HgCl_2$ for TA and DIC, acidified for sulfate, and stored

173 at 4 °C until analysis in the laboratory. Total alkalinity was measured by open cell titration with 0.01

174 M HCl (Dickson et al., 2007). DIC concentrations were analyzed with a DIC analyzer

175 (Apollo/SciTech®) on 1 ml samples as previously described (Rassmann et al., 2016). The TA and DIC

176 methods were calibrated using certified reference materials for oceanic CO_2 measurements provided

177 by the Scripps Institution of Oceanography (batch n°136). The relative uncertainty for both DIC and

178 TA was ± 0.5 % of the final value. Sulfate concentrations were quantified after dilution by ion

179 chromatography on an ICS 1000 chromatograph (Dionex) with an IonPac AS 9 HC column and AG

180 9 HC guard by suppressed conductivity with an AERS 500 suppressor (ThermoFisher Scientific). A

181 9 mM solution of Na_2CO_3, at a flow rate of 1 ml min^{-1} was used as the eluent. The relative uncertainty

182 of this method was ± 1.6 %. Separate pore water fractions were frozen at -18 °C for sulfate analysis

183 by high performance liquid chromatography using a Waters, Inc. 1525 binary pump with Waters 2487

184 absorbance detector at 215 nm and a Metrohm Metrosep A Supp 5 anion exchange column (150 mm

185 x 4.0 mm) with a 1.0 mM $NaHCO_3$ / 3.2 mM Na_2CO_3 eluent at a flow rate of 0.7 ml min^{-1} (Beckler

186 et al., 2014). To measure ammonium (NH^+_4) concentrations, samples were diluted and analysed using

187 the indophenol blue method (Grasshof et al., 1983). The uncertainty of the method was about 5 %.

188 Pore water fractions were also acidified with 2 % HCl for Ca^{2+} analysis by inductively-coupled

189 plasma atomic emission spectroscopy (Ultima 2, Horiba Scientific). The method was validated with

190 mono-elemental standards and standard solutions (IAPSO, CASS-4, and NASS-6 seawater reference

191 materials) and displayed an external relative uncertainty of ± 2-3 % depending on the sample series.

192   Close to the Rhône River mouth, at station A, Z, and AK, one core was subsampled from the side

193   with 1cm diameter corers made of cut 10-ml syringes every 5 cm through pre-drilled holes. The

194   content of these subsamples was carefully inserted in gas tight vials containing deionized water and

195    $HgCl_2$ solution and kept at 4°C until methane analysis. Dissolved methane was quantified after

196   degassing of the pore waters into the headspace and quantified by gas chromatography with a relative

197   uncertainty of ± 5 % (Sarradin and Caprais, 1996). The position of the sulfate-methane transition zone

198   (SMTZ) was determined as the zone around the depth where $[SO_4^{2-}] = [CH_4]$ (Komada et al., 2016).

199   Finally, acid volatile sulfur (AVS) for the determination of FeS_s was extracted from the same sediment

200   used for the pore water extractions and conducted in triplicate by cold acid distillation of H_2S (g)

201   under anoxic conditions that was trapped by NaOH and quantified voltammetrically (Henneke et al.,

202   1991).

203   *2.7 Nanoparticulate FeS and ion activity product for FeS precipitation*

204   As a significant fraction of FeS nanoparticles may pass through the rhizon filters (0.1μm) used

205   to extract pore waters (Nakayama et al., 2016) and the ferrozine method is well known to dissolve

206   FeS nanoparticles (Davison et al., 1998), the difference between spectrophotometrically-determined

207   Fe^{2+} concentrations ($[\Sigma Fe^{2+}]_{FR}$) and electrochemically-determined Fe^{2+} concentrations ($[Fe^{2+}_{echem}]$) in

208   the pore waters was attributed to FeS nanoparticles (FeS_0), as demonstrated previously (Bura-Nakic

209   et al., 2009; Eq. 2).

$$[FeS_0] = [\sum Fe^{2+}]_{FR} - [Fe^{2+}_{echem}] \tag{2}$$

210   In this interpretation, FeS_0 nanoparticles encompass both the molecular clusters of FeS (FeS_{aq})

211   detected electrochemically, which must be smaller than 5 nm in diameter to diffuse to the electrode

212   (Buffle, 1988), and the larger FeS nanoparticles that are not detected voltammetrically. The ionic

213   activity product (IAP) for the precipitation of FeS was calculated using Eq. 3 (Beckler et al., 2016),

$$pIAP = \log(\frac{\gamma_{Fe(II)}[Fe^{2+}]\gamma_{HS}\alpha_{HS}\Sigma H_2 S}{\{H^+\}}) \tag{3}$$

214 where $\gamma_{Fe(II)}$ and γ_{HS} represent the activity coefficients of Fe^{2+} and HS^{--}, $\alpha_{HS} = \frac{\{H^+\}K_{a1}}{\{H^+\}^2 + \{H^+\}K_{a1} + K_{a1}K_{a2}}$

215 is calculated with the acid dissociation constant of H_2S ($K_{a1} = 10^{-6.88}$) and HS^- ($K_{a2} = 10^{-17}$) (Davison,

216 1991), and $\{H^+\}$ is the activity of the proton. Activity coefficients of Fe^{2+} (Millero and Schreiber,

217 1982) and HS^- (Millero, 1983) were calculated using Pitzer parameters.

218 *2.8 Calculations of oxygen uptake and AVS burial rates*

219   Diffusive oxygen uptake (DOU) fluxes were calculated using Fick's first law (Berner, 1980, Eq.

220 4),

$$DOU = -\emptyset \cdot D_S \cdot \frac{d[O_2]}{dz}\Big|_{z=0} \tag{4}$$

221 where ϕ is the sediment porosity, D_s is the apparent diffusion coefficient in the sediments, and

222 $\frac{d[O_2]}{dz}\Big|_{z=0}$ is the oxygen gradient at the SWI. The D_s coefficients were adjusted for diffusion in a porous

223 environment according to: $D_S = \frac{D_0}{(1 + 3 \cdot (1-\emptyset))}$ with the diffusion coefficient in free water (D_0) chosen

224 according to Broecker and Peng (1974) and recalculated to *in situ* temperature by the Stokes-Einstein

225 relation (Li and Gregory, 1974).

226   AVS burial fluxes were estimated using available sedimentation rates (ω from Charmasson et al.

227 (1998) and Miralles et al. (2005)), average AVS concentrations and porosities of each sediment core,

228 according to Eq. 5,

$$AVS_{burial} = (1-\emptyset) \cdot \omega \cdot AVS \cdot \rho \tag{5}$$

229 where ϕ is the sediment porosity, ω the sedimentation rate, and ρ the sediment dry bulk density.

230 *2.9 Stoichiometric ratios*

231   To determine the relationship between net TA and DIC production and to establish whether

232 sulfate reduction represents the main source of TA and DIC in these sediments, stoichiometric ratios

233 of the relative production of TA compared to DIC (r_{AD}), as well as TA (r_{AS}) and DIC (r_{DS}) compared

234 to sulfate consumption, were calculated from the pore water data and compared to theoretical ratios

235 from the reaction stoichiometries (Table 1). Experimental stoichiometric ratios were obtained from

236 the slope and standard deviation of the linear regression of TA, DIC, and sulfate property-property

237 plots of concentration changes with respect to bottom water concentrations at each depth in the pore

238 waters (ΔTA, ΔDIC and ΔSO_4^{2-}) relative to each other after correcting for differences in TA, DIC and

239 sulfate diffusion in the sediments (Berner, 1980, Eq. 6),

240
$$r_{ij} = \frac{D_i \cdot \Delta i}{D_j \cdot \Delta j}$$
(6)

241 where i is the concentration of either TA or DIC, j the concentration of SO_4^{2-} or DIC and D_i and D_j

242 are the corresponding diffusion coefficients. At the pH of the pore waters (pH ~ 7.5), more than 95 %

243 of DIC and carbonate alkalinity are composed of bicarbonate ion (HCO_3^-). Given the relatively small

244 difference in the diffusion coefficients of HCO_3^- and CO_3^{2-} (11.8 and 9.55 x 10^{-6} cm^2 s^{-1} at 25°C, Li

245 and Gregory, 1974) and the high proportion of HCO_3^- relative to CO_3^{2-}, the diffusion coefficient of

246 HCO_3^- was adopted for both TA and DIC diffusion.

247   The effect of the precipitation or dissolution of calcium carbonate on TA and DIC variations was

248 also accounted for by considering the Ca^{2+} concentration gradients in the pore waters. For these

249 calculations, the absolute value of the Ca^{2+} concentration relative to its bottom water concentration

250 (ΔCa^{2+}) was added to the ΔTA or ΔDIC after taking the corresponding diffusion coefficients into

251 account ($D_{TA}\Delta$ TA + $2D_{Ca}|\Delta Ca^{2+}|$ for alkalinity and $D_{DIC}\Delta$ DIC + $D_{Ca}|\Delta Ca^{2+}|$ for DIC) and plotted

252 against $D_{SO42}\cdot\Delta SO_4^{2-}$. The calculated slope provided a stoichiometric ratio corrected for the

253 precipitation of calcium carbonate (r_{IJc}). Pore water saturation states, regarding Calcite (Ω_{Ca}), were

254 calculated according to the equation proposed by Mucci (1983) and Millero (1995).

3.Results

3.1 Bottom water and surface sediment characteristics

257   At all stations, bottom water salinities ranged from 37.5 to 38.0 and temperatures varied from

258 14.7 to 20.6 °C (Table 2). Total alkalinity and DIC concentrations (average TA = 2.60 ± 0.01 mM and

259 average DIC = 2.30 ± 0.02 mM, Table 2) were relatively high compared to the Mediterranean Sea

260 average, but common for the Gulf of Lions (Cossarini et al., 2015). The pH_T of the bottom waters

261 varied from 8.05 to 8.09 with the highest value observed at station AK and the lowest at station E.

262 Although the oxygen concentration decreased with water depth, bottom waters were always well

263 ventilated, with dissolved O_2 concentrations higher than 220 µmol L^{-1}. Sediment porosity ranged

264 between 0.7 and 0.8 at the SWI, and they were similar at all stations between 20 and 400 mm depth

265 (Table 2).

266 *3.2 Benthic total and diffusive fluxes*

267   The *in situ* pH and O_2 microprofiles reflected the differences between the three study domains

268 under the influence of the Rhône River plume (Fig. 2). In the proximal zone (stations A and Z), the

269 oxygen penetration depth was only 1.5 to 2.5 mm into the sediment as also indicated by separate

270 voltammetric measurements (Fig. 5). The oxygen penetration depth increased from 2 to 6 mm at

271 station K and reached 8 to 11 mm at the most offshore station E. As a result of bad weather conditions,

272 no exploitable *in situ* microprofiles were recorded at stations AK and B, though *ex situ* voltammetric

273 profiles determined oxygen penetration depths of 4 and 2 mm, respectively (Fig. 5). All pH microfiles

274 indicated a pH minimum between 7.2 and 7.4 just below the OPD followed by an increase to between

275 7.5 and 7.6 in the manganous/ferruginous layers of the sediment around 5 mm inshore and below 12

276 mm offshore (Fig. 2). Below this depth, pH stabilizes.

277   The benthic chamber was deployed once at stations A and E and twice at station Z (Z' is the

278 replicate). Total alkalinity and DIC concentrations increased linearly with time in the chamber, but

279 concentration changes decreased along the nearshore-offshore transect (Fig. 3). The highest benthic

280 fluxes were recorded for the two deployments at station Z, with TA fluxes of 73.9 ± 20.6 and 56.0 ±

281 17.8 mmol m^{-2} d^{-1} and DIC fluxes of 78.3 ± 10.9 and 37.2 ± 7.2 mmol m^{-2} d^{-1} (Fig. 4, Table 2). At

282 station A, the benthic TA and DIC fluxes reached lower values of 14.3 ± 1.6 and 17.8 ± 1.6 mmol m^{-}

283 ^{2} d^{-1}, respectively, while benthic fluxes were lowest at station E, with a TA flux of 3.7 ± 0.9 mmol m^{-}

284   ^{2} d^{-1} and a DIC flux of 9.9 ± 0.9 mmol m^{-2} d^{-1}. In parallel, DOU fluxes reached 10.2 ± 1.3 and 10.4

285   ± 0.9 mmol m^{-2} d^{-1} at stations A and Z and decreased offshore to 5.9 ± 1.0 mmol m^{-2} d^{-1} at station K

286   and 3.6 ± 0.6 mmol m^{-2} d^{-1} at station E (Fig. 4, Table 2). Although the relative importance of DOU

287   compared to TA and DIC fluxes increased offshore, the TA and DIC fluxes were always between 2

288   and 8 times larger than the DOU fluxes (Fig. 4).

289   *3.3 Electrochemistry profiles*

290   Dissolved Fe^{2+} concentrations as a function of depth in the sediment mirrored the voltammetric

291   signals of soluble organic-Fe(III) complexes at stations A, Z, AK, B, and K (Fig. 5). High

292   concentrations of dissolved Fe^{2+} were observed in the proximal domain at stations A (341 ± 22 µM)

293   and Z (234 ± 25 µM), where dissolved ΣH$_2$S was not detected (Fig. 5). At station AK, the shallowest

294   station in the prodelta domain, dissolved Fe^{2+} increased to a maximum concentration of 255 µM

295   around 2 cm depth, then decreased with sediment depth as FeS$_{aq}$ below 6.5 cm and small

296   concentrations of dissolved ΣH$_2$S around 17 cm were produced (Fig. 5). The two deeper prodelta

297   stations, B and K, displayed lower Fe^{2+} concentrations, including one peak not exceeding 81 µM

298   (station B) or 73 µM (station K) in the top 2 cm of the sediment and a second peak not exceeding 50

299   µM between 12-14 cm (station B) and 86 µM between 5-7.5 cm (station K) in the sediment. Although

300   FeS$_{aq}$ was only detected below 15 cm at station K, ΣH$_2$S was produced in low concentrations (< 5

301   µM) around 6.5 cm at stations B and K (Fig. 5). A peak of Fe^{2+} was initially formed in the top 5 cm

302   of the distal domain (station E) but decreased to a minimum value with depth and did not correlate

303   with the organic-Fe(III) voltammetric signals, which also remained low throughout the profile (Fig.

304   5). Finally, station E displayed generally low concentrations of ΣH$_2$S in the pore waters (< 6 µM),

305   though the onset of ΣH$_2$S production was much shallower (2.5 cm) and ΣH$_2$S concentrations were

306   consistently higher throughout the profile than at any other stations.

307 *3.4 Geochemical characteristics of the pore waters and sediments*

308 Both TA and DIC concentrations increased rapidly within the pore waters (Fig. 6), likely reflecting

309 the intensity of organic carbon mineralization rates in these sediments. At all stations, DIC pore water

310 concentrations correlated well with TA (overall slope: 1.01 ± 0.006, $r^2=0.995$, n=134). The TA and

311 DIC gradients were highest at stations A and Z, where maximum concentrations of both species

312 reached around 55 mM. At station AK, TA and DIC concentrations reached a maximum of 15 mM at

313 25 cm depth but decreased to 6 mM at the bottom of the core. The maximum concentrations of TA

314 and DIC of 35 mM observed at station B, were more comparable to the stations in the vicinity of the

315 river mouth (stations A and Z) than other stations located in the prodelta domain (stations AK and K).

316 At station K, TA and DIC concentrations reached 10 mM, whereas the lowest TA and DIC gradients

317 were measured at station E, with concentrations reaching only 4.6 mM at the bottom of the cores (30

318 cm). Sulfate was completely removed from the pore waters at depths of 35, 24, and 45 cm at station

319 A, Z, and B, respectively (Fig. 6). In turn, sulfate concentrations decreased to a minimum

320 concentration of 20 mM at 29 and 24 cm depth at stations AK and K, whereas sulfate consumption

321 was much smaller at station E with a minimum concentration of 28 mM (bottom water sulfate

322 concentration was 31.4 mM). As a result, TA and DIC changes in concentration at a given depth were

323 highly inversely correlated ($r^2 > 0.97$) with sulfate changes in concentration at stations A, Z, AK, B,

324 and K (Table 3). At station E, sulfate variations in the observed depth were in the same order of

325 magnitude as the measuring uncertainties. Simultaneously, TA and DIC demonstrated strong

326 correlations ($r^2 > 0.97$) at stations A, Z, AK, B, and K (Table 3). In the proximal domain (stations A

327 and Z), ammonium increased with sediment depth to concentrations > 3 mM (Fig. 6). At station B,

328 ammonium reached concentrations > 2 mM with depth, whereas ammonium concentrations did not

329 exceed 1.5 mM at station AK, 0.6 mM at station K, and 0.3 mM at station E. At all stations nitrite

330 plus nitrate concentrations were less than 20 μM (data not shown). Significant methane

331 concentrations (> 50 μM) were detected at the bottom of the sediment core at stations A, Z, and AK

332 (Fig. 6), and a SMTZ was identified between 28 and 39 cm at station A and between 19 and 39 cm at

Biogeosciences
Discussions

333   station Z. As methane was < 50 µM throughout the profile at station K and sulfate was not completely

334   consumed inside the sediment core at station AK, the SMTZ was not determined at these two stations.

335   Methane analyses were not carried out for the other stations.

336   The sediment pore waters were oversaturated with respect to calcite ($\Omega_{Ca} > 1$) at all stations. At

337   stations A, Z, and B, decreasing Ca^{2+} concentrations in the pore waters indicated precipitation of

338     $CaCO_3$, whereas Ca^{2+} concentrations remained close to the bottom water Ca^{2+} concentrations (11.2

339   mM in Mediterranean waters) at the other stations (Fig. 6). Dissolved phosphate concentrations

340   (ΣPO_4^{3-}) were relatively high (50-100 µM) throughout the profiles at stations A, AK, K and Z, and a

341   large increase in concentration (up to 160 µM at station Z) was observed at station AK, K and Z

342   between 15 and 22 cm. In turn, ΣPO_4^{3-} production was minimal throughout station E pore waters (<

343   10 µM). Dissolved phosphate was not measured at station B. Sediment samples were analyzed for

344   AVS as a function of depth at stations A, AK, and E to assess one station in each domain (Fig. 6). At

345   station A, a peak in AVS (65 µmol g^{-1}) was measured around 8.0 cm followed by a second, smaller

346   peak (22 µmol g^{-1}) at 14 cm, after which AVS decreased with depth. The AVS concentrations were

347   low in the top portion of the sediment at station AK but increased with depth to 100 µmol g^{-1} around

348   15 cm. At station E, only a small AVS peak of 20 µmol g^{-1} was observed at 14 cm. Finally, large

349   concentrations of FeS nanoparticles (FeS_0) were found in the proximal and prodelta stations,

350   including two broad peaks and maximum concentrations around 1 mM at stations A and Z and a large

351   subsurface maximum up to 6 mM at 145 mm at station AK. These FeS_0 concentrations increased as

352   a function of depth to a relatively constant 0.5 mM below 4.5 cm at station B and below 12 cm at

353   station K, whereas they remained mostly negligible at station E (Fig. 6).

354   **4. Discussion**

355   In this study, we want to relate biogeochemical processes in the sediment to the observed TA and

356   DIC fluxes. Firstly, benthic TA and DIC fluxes in the Rhône River prodelta are compared to other

357   similar systems to evaluate their relative importance. In the following sections, the most likely

358   biogeochemical processes responsible for the high TA flux are identified based on the sediment depth

359   profiles collected. In particular, the role of iron sulfide mineral precipitation on the benthic TA flux is

360   established using a variety of analytical techniques, speciation calculations, and a mass balance

361   approach. Finally, the link between inputs to the sediment, carbon mineralization processes, sulfide

362   mineral burial, and the benthic TA flux is provided using a conceptual model.

363   *4.1 DIC and alkalinity fluxes from the sediment*

364   The sediments of the Rhône proximal and prodelta zones represent important sources of both

365   DIC and TA to the bottom waters (Fig. 4). The DIC fluxes observed in the proximal domain (18-78

366   mmol m^{-2} d^{-1} at station A and Z; Fig. 4) are in the range of previously measured fluxes in other deltas

367   where anaerobic mineralization processes are dominant, including Mississippi delta sediments from

368   core incubations (15-20 mmol m^{-2} d^{-1}; Lehrter et al., 2012) or benthic chambers (36-53 mmol m^{-2} d^{-}

369   ^{1}; Rowe et al., 2002), benthic chamber measurements of the Po River delta sediments and the Adriatic

370   shelf (15-25 mmol m^{-2} d^{-1} ; Hammond et al., 1999), or the Fly River delta during the most active

371   season (35-42 mmol m^{-2} d^{-1} ; Aller et al., 2008) and near the Guadalquivir River estuary (36-46 mmol

372   m^{-2} d^{-1}, Ferron et al., 2009). In contrast, fewer alkalinity fluxes were measured in river deltas, though

373   those obtained from benthic chambers in the Danube and Dniester deltas in the Northwest Black Sea

374   (21-67 mmol m^{-2} d^{-1}, Friedl et al., 1998), are within the range of values reported in this study (14-74

375   mmol m^{-2} d^{-1}). Benthic TA fluxes obtained in the Guadalquivir estuary (24-30 mmol m^{-2} d^{-1}; Ferron

376   et al., 2009) and the Adriatic shelf sediments off the Po River delta (0.5-10.4 mmol m^{-2} d^{-1}; Hammond

377   et al., 1999) are in the lower range of TA fluxes measured in the present study. The biogeochemical

378   origin of these TA benthic fluxes is discussed in the next sections.

379   *4.2 The relative importance of nitrification/denitrification on the TA budget*

380   Denitrification is known as a benthic TA source to the bottom waters as 0.8 moles of TA are

381   produced for 1 mole of organic carbon oxidized by nitrate and the product N$_2$ does not react further

382 with dissolved oxygen (Table 1, Eq. 5; Thomas et al., 2009; Krummins et al., 2013; Brenner et al.,

383 2016). Published estimates of total denitrification rates in Rhône prodelta and shelf sediments range

384 between 4 mmol m^{-2} d^{-1} in the proximal zone to 1 mmol m^{-2} d^{-1} in the continental shelf (Pastor et al.,

385 2011). Conversion to alkalinity flux would provide a range between 0.8 and 3.2 mmol TA m^{-2} d^{-1}. As

386 such, denitrification would account for < 10% of the TA flux in the proximal zone where substantial

387 fluxes were measured by *in situ* benthic chambers (Fig. 4). Furthermore, the only net production of

388 TA by denitrification must be related to external nitrate sources as nitrification (overall oxidation of

389 ammonium to nitrate) consumes 2 moles of TA per mole of ammonium transformed into nitrate (Table

390 1, Eq. 2; Hu et al., 2011a). As coastal sediments mostly display coupled nitrification-denitrification,

391 this process does only represent a small source of TA to the bottom waters (Brenner et al., 2016). It

392 can therefore be concluded that the contribution of denitrification to TA fluxes is minimal in the

393 proximal zone and could be proportionally more important on the shelf where TA fluxes are much

394 lower.

4.3 DIC and TA produced by sulfate reduction

396 Sulfate reduction typically represents a major organic carbon mineralization pathway in organic-

397 rich sediments that simultaneously produces two moles of total alkalinity (TA) and two moles of DIC

398 per mole of sulfate (Table 1, Eq. 6) (Canfield et al., 1993b; Burdige, 2011). Dissimilatory iron

399 reduction (Table 1, Eq. 7) in turn produces 1/4 moles of DIC and consumes 7/4 moles of H$^+$, resulting

400 in two moles of TA produced per mole of Fe. As these two processes equally produce two moles of

401 TA per mole of terminal electron acceptor (Table 1, Eq.6 for SO$_4^{2-}$ and Eq. 7 for Fe(OH)$_3$), they can

402 both contribute significantly to the bulk alkalinity production in sediment pore waters. The low

403 concentration of nitrate, relatively low production of reduced metals in the pore waters (Fig. 5), and

404 intense ammonium and DIC production in parallel with sulfate consumption at depth (Fig. 6) confirm

405 that sulfate reduction is one of the dominant mineralization pathways in the Rhône prodelta sediments

406 (Pastor et al., 2011; Rassmann et al., 2016). Experimentally-derived stoichiometric ratios of the

407 relative production of DIC and TA compared to sulfate consumption may indicate the dominant

408 reaction pathways responsible for the high alkalinity generated in these sediments (Burdige and

409 Komada, 2011). Factoring carbonate precipitation using the pore water Ca^{2+} data, the r_{DSc} were

410 determined to range between -2.05 and -1.86, except for one value at -1.37 (station B), whereas the

411 r_{ASc} ratios ranged between -2.35 and -1.89 with the exception of station B at -1.58 (Table 3).

412 Theoretically, the r_{DS} and r_{AS} should equal -2.0 if sulfate reduction is the only control on DIC and TA

413 production (Table 1, Eq. 6), suggesting that, except at station B, the influence of other diagenetic

414 processes on r_{ASc} and r_{DSc} is limited. At station B, however the higher r_{DSc} ratio (Table 3) may indicate

415 significant anaerobic oxidation of methane (AOM Table 1, Eq. 8) which generates a theoretical r_{DS}

416 of -1 (Borowsi et al., 1996; Komada et al., 2016). Unfortunately, methane sampling was not

417 performed at station B, preventing precise identification of AOM at this station.

4.4 Formation of iron sulfide species

419 Although the complete depletion of sulfate in the first 30 cm of the sediment at stations A, Z, and

420 B implies an equivalent production of dissolved sulfide (ΣH_2S) (Table 1, Eq. 6), pore waters displayed

421 little to no ΣH_2S (Fig. 5). If all of the produced ΣH_2S diffused upward and reacted in the oxic sediment

422 layer, the alkalinity produced by sulfate reduction would be consumed by the oxidation of ΣH_2S by

423 dissolved O_2 and the pH should be lowered significantly given the large acidity generated by this

424 reaction (Table 1, Eq. 4). Although ΣH_2S was nearly absent of the pore waters (Fig. 5), the pH

425 minimum was never lower than 7.2 and the observed alkalinity fluxes across the SWI were substantial

426 (Fig. 4), indicating that ΣH_2S was removed from the pore waters below the oxic layer. Abiotic

427 reduction of Fe(III) oxides by ΣH_2S (Table 1, Eq. 9), followed by precipitation of FeS in the anoxic

428 zone (Table 1, Eq. 10; Berner, 1970; Pyzik and Sommer, 1981; Carman and Rahm, 1997, Soetaert et

429 al., 2007), and eventually formation of pyrite (Table 1, Eq. 11; Rickard and Luther, 1997) may

430 represent a significant ΣH_2S removal pathway. As the abiotic reduction of Fe(III) oxides by ΣH_2S

431 coupled with either FeS or FeS and pyrite precipitation (Table 1, Eq. 9-11) does overall not alter

432 alkalinity, bacterial sulfate reduction followed by abiotic precipitation of iron and sulfide from the

433 pore waters to either FeS or pyrite (Table 1, Eqs. 12 and 13) should result in $r_{AD} = 1$ and $r_{DS} = r_{AS} = -$

434 2. Formation of pyrite is accompanied by the consumption of molecular H_2 by sulfate-reducing

435 bacteria, resulting in a slight increase in the r_{AD} and r_{DS} to 1.1 and -1.81 for the overall reaction while

436 the r_{AS} ratio should not change (Table 1, Eq. 14). Another possible pathway includes the concomitant

437 production of Fe^{2+} by dissimilatory iron reduction (Table 1, Eq. 7) and $\Sigma H_2 S$ by sulfate reduction

438 followed by precipitation of FeS. In this case, the net r_{AD} and r_{DS} ratios should decrease to 0.89 and -

439 2.25, whereas the r_{AS} ratio should remain at -2 (Table 1, Eq. 15). With ensuing formation of pyrite,

440 theoretical mole ratios may change slightly to $r_{AD} = 0.94$ and $r_{DS} = -2.13$ without H_2 reoxidation (Table

441 1, Eq. 16), whereas r_{AD} and r_{DS} ratios of 1.06 and -1.89 should be reached with H_2 reoxidation by

442 sulfate-reducing bacteria (Table 1, Eq. 17). In both cases, the r_{AS} ratio should remain at -2.

443   The observed range of r_{ADc} (1.06 to 1.15) and r_{DSc} (-2.05 to -1.86) ratios in the proximal and

444 prodelta stations, except at station B (Table 3), is fully compatible with sulfate reduction coupled to

445 iron reduction and FeS precipitation (possibly followed by pyritization), though r_{ADc} and r_{DSc} ratios

446 are not able to distinguish abiotic and microbial pathways of iron reduction. The occurrence of

447 dissimilatory iron reduction in the proximal and prodelta domains, however, is substantiated by

448 several other pieces of evidence. First, the production of soluble organic-Fe(III) complexes deeper

449 than the oxygen penetration depths (Fig. 5) indicates that these species did not result from the

450 oxidation of Fe^{2+} by dissolved O_2 in the presence of organic ligands (Taillefert et al., 2000). Second,

451 as soluble organic-Fe(III) complexes are produced as intermediates in the reduction of Fe(III) oxides

452 by iron reducing bacteria (Taillefert et al., 2007; Jones et al., 2010), their concomitant detection with

453 Fe^{2+} at all the stations in the proximal and prodelta domains (Fig. 5) suggests they were produced

454 during dissimilatory iron reduction. Third, the positive correlation between the current intensities of

455 organic-Fe(III) complexes and Fe^{2+} concentrations is in line with the same correlation obtained in

456 iron-rich deep-sea sediments (Fig. 7) where sulfate reduction was not significant (Beckler et al.,

457 2016). Finally, as these organic-Fe(III) complexes are readily reduced by $\Sigma H_2 S$ (Taillefert et al.,

458 2000), their presence in zones of sulfate reduction suggest these sediments are highly dynamic with

459 periods of intense sulfate reduction alternating with periods during which sulfate reduction is

460 repressed and replaced by microbial iron reduction. These dynamics may be controlled by the input

461 of organic and inorganic material from the Rhône River in the proximal domain, especially during

462 floods when most of the solid material is deposited on the seafloor (Cathalot et al., 2010; Pastor et

463 al., 2018).

464 *4.5 FeS precipitation*

465 The discrepancy between sulfate consumption and the low concentration of ΣH_2S along with the

466 high TA fluxes clearly suggest that much of the sulfur was precipitated in the solid phase. Indeed,

467 AVS measurements show precipitation of FeS in the proximal and prodelta domains (Fig. 6). In

468 addition, the large phosphate concentrations observed at depth in the proximal and prodelta domains

469 (Fig. 6) suggest that ΣPO_4^{3-} adsorbed to Fe(III) oxides was released in the pore waters during

470 secondary conversion of Fe(III) oxides to FeS (Anschutz et al., 1998; Rozan et al., 2002). More

471 importantly, large concentrations of nanoparticulate FeS (FeS_0 in the range of 1-6 mM) were

472 identified in the proximal and prodelta stations that decreased with distance from shore (Fig. 6). The

473 existence of FeS_0 suggests that large fractions of Fe^{2+} and ΣH_2S were actively removed from the pore

474 waters at the time of measurements and eventually immobilized under the form of sulfide minerals.

475 Although soluble FeS_{aq} clusters detected electrochemically when the system is oversaturated with

476 respect to FeS (Theberge and Luther, 1997) are considered good indicators of the active precipitation

477 of iron sulfide minerals (Luther and Ferdelman, 1993; Davison et al., 1998; Taillefert et al., 2000),

478 they were rarely observed in the Rhône River delta (Fig. 5). Indeed, the ion activity products (pIAPs)

479 calculated at most stations indicate that pore waters were either undersaturated, as a result of the low

480 concentrations (stations AK, B, and K) or complete absence (stations A and Z) of dissolved sulfides,

481 or close to the solubility of amorphous FeS or mackinewite (Fig. 8). Collectively, the large

482 concentrations of dissolved FeS_0 compared to the small electrochemically active FeS_{aq} complexes

483 and the generally low saturation state of the pore waters indicate that FeS was much more aggregated

484 during this time period. Overall, the presence of soluble organic-Fe(III) complexes along with

485 dissolved Fe^{2+} throughout the profiles, the absence of ΣH_2S and FeS_{aq}, and the large concentrations

486 of dissolved FeS_0 found in the pore waters despite complete removal of sulfate in the proximal and

487 some of the prodelta stations provide strong evidence of large FeS precipitation in a context where

488 sulfate-reducing conditions may alternate with iron-reducing conditions as already observed

489 seasonally in estuarine sediments (Taillefert et al., 2002).

490 *4.6. Benthic alkalinity flux as a result of iron sulfide burial*

491   As the extreme sedimentation rates (> 30 cm yr^{-1}) in the proximal domain prevent short-term

492 reoxidation of ΣH_2S, the burial of FeS should represent a net source of alkalinity in the pore waters

493 (Berner, 1982; Hu and Cai, 2011a; Brenner et al., 2016). With the precipitation of FeS, about 2 to 3

494 moles of alkalinity equivalent should be produced for each mole of sulfur precipitated (Table 1, Eqs.

495 12 and 15). Assuming concomitant dissimilatory iron and sulfate reduction dominate in the proximal

496 and prodelta zones, a conservative ratio of 2 moles of TA equivalent per mole of FeS precipitated can

497 be estimated (Table 1, Eq. 15). In this calculation, the alkalinity production flux was estimated from

498 the average AVS burial fluxes using Eq. 5, with the caveat that these flux comparisons are made

499 assuming steady-state which is questionable in such a dynamic system. Nonetheless, the average AVS

500 concentration of the proximal station (station A) was used, as the sedimentation rate at this station is

501 so high (>30 cm y^{-1}) that the entire sediment layer investigated is buried rapidly in a year. The

502 calculated AVS burial flux provides an alkalinity-equivalent flux of 25.0 ± 7.7 mmol m^{-2} d^{-1} in the

503 proximal domain (Table 4), which falls within the range of benthic alkalinity fluxes measured by

504 benthic chamber at stations A and Z (14.3 - 73.9 mmol m^{-2} d^{-1}; Fig. 4 and Table 4). In the prodelta,

505 the alkalinity-equivalent flux is estimated at 9.8 ± 2.8 mmol m^{-2} d^{-1} at station AK (Table 4), which

506 unfortunately cannot be compared to benthic alkalinity fluxes as they were not measured. In the distal

507 domain, however, a low alkalinity-equivalent flux of 0.04 ± 0.1 mmol m^{-2} d^{-1} is estimated from the

508   average AVS burial flux at station E. This flux is much lower than the 3.7 ± 0.9 mmol m^{-2} d^{-1} flux

509   measured by benthic chamber (Fig. 4), a difference that could be due to denitrification and shallow

510   carbonate dissolution.

511   4.7. Benthic alkalinity flux as a result of carbonate dissolution

512   Calcium carbonate dissolution below the sediment-water interface as a result of the acidity

513   generated by aerobic respiration may represent another possible contributor to TA fluxes as

514   demonstrated in carbonate-rich permeable sediments (Burdige and Zimmerman, 2002; Cyronak et

515   al., 2013; Rao et al., 2014). Both the water column ($\Omega_{Ca} = 5.5$) and the pore waters ($\Omega_{Ca} > 1$) of the

516   proximal zone are largely oversaturated with respect to calcite (Rassmann et al., 2016; Fig. 6). These

517   findings are corroborated by a large decrease in Ca^{2+} concentration in the pore waters, indicating

518   CaCO$_3$ precipitation at depth in proximal zone sediments. Yet, the intense consumption of dissolved

519   oxygen in the first millimeters below the sediment-water interface generates a large pH decrease (Fig.

520   2) that may induce carbonate dissolution at this scale. Calcium carbonate saturation states at a

521   millimeter scale near the SWI were calculated from pH profiles and an interpolation of the centimetre-

522   scale DIC profiles using the SeaCarb software (Fig. 9). They show that in the proximal zone, the

523   saturation state with respect to calcite, which is the most abundant detrital carbonate in these

524   sediments (Rassmann et al., 2016), is always above 1.5. Such saturation state precludes massive

525   carbonate dissolution at the sediment surface and discounts shallow carbonate dissolution as playing

526   a large role on the benthic alkalinity fluxes observed in the proximal sediments. Minor quantities of

527   calcium carbonate may be dissolved in microniches where the pH could be lower than 7.4 or less

528   abundant carbonate forms (aragonite) may dissolve in the millimetric layers where this mineral is

529   close to undersaturation. These processes, however, surely represent an insignificant flux in the

530   proximal zone compared to the large alkalinity generated by sulfate reduction and subsequent FeS

531   burial. At the distal station on the shelf (Station E, Fig. 9c), the saturation state was close to 1 which

532   may indicate a potential contribution of calcium carbonate dissolution to the benthic alkalinity flux.

4.8. Linking TA and DIC fluxes to mineralization processes

533

534   Overall, the present findings indicate that FeS burial modifies the alkalinity budget in the

535   proximal and prodelta sediments (Brenner et al., 2016). As the order of magnitude of the measured

536   benthic alkalinity fluxes is compatible with the alkalinity generated during the reduction of Fe(III)

537   oxides, sulfate, and subsequent FeS burial in the proximal zone, these processes are likely responsible

538   for the large alkalinity fluxes reported in this high-sedimentation delta and, potentially, other similar

539   systems (Hu and Cai, 2011a).

540   The biogeochemical cycling of C, Fe, S, and TA close to the Rhône River mouth can be

541   theoretically summarized as follows (Fig. 10): (i) the high pore water DIC concentrations resulting

542   from the production of metabolic CO_2 during organic carbon mineralization lead to benthic DIC

543   fluxes that are only modulated by the precipitation of carbonate minerals; (ii) the high pore water TA

544   concentrations result from intense iron and sulfate reduction as a result of the high supply of organic

545   matter and Fe(III) oxides to the sediment; (iii) the precipitation of FeS and the high sedimentation

546   rates near the river mouth preserve the majority of reduced iron and ΣH_2S buried in the form of FeS

547   minerals and potentially pyrite within the anoxic sediments (Aller et al., 1986); and (iv) ultimately,

548   the TA-consuming reoxidation of reduced metabolites (i.e., NH_4^+, ΣH_2S, Fe^{2+}) is not important in the

549   oxic sediment layers, and a significant fraction of the anaerobically-produced TA is transferred across

550   the SWI (Fig. 10, red dashed line). In these conditions, anaerobic and aerobic processes are

551   decoupled, and the consumption of oxygen no longer reflects the overall respiration rates within these

552   sediments (Pastor et al., 2011) as observed by the relatively lower contribution of DOU fluxes

553   compared to TA and DIC fluxes in the proximal domain (Fig. 4).

554   In contrast, sedimentation rates (Table 2), overall respiration rates (Fig. 4), and the intensity of

555   iron and sulfate reduction (Fig. 6) decrease in the distal domain (station E), and as a consequence the

556   relative proportion of aerobic processes increases (Pastor et al., 2011). Despite the relatively small

557   decrease in pore water sulfate concentrations with depth and low ΣH_2S concentrations (< 10 µmol L$^-$

558   ^{1}) at the most offshore station E, ΣH_2S concentrations were the highest of all the stations. These

559 findings likely reflect the fact that less riverine Fe(III) oxides were available for FeS precipitation.

560 With low sedimentation rates (0.1 to 1 cm yr^{-1}) and thus low input of organic matter and Fe(III)

561 oxides, the overall carbon turnover is decreased and the reduced by-products of sulfate and/or iron

562 reduction may be transported back to the oxic sediment layers to be reoxidized by dissolved oxygen.

563 In this case, the alkalinity generated by anaerobic respiration processes is consumed by reoxidation

564 of the reduced metabolites, and the flux of alkalinity near the SWI decreases to weak values at station

565 E (Fig. 4 and Fig. 10, black line).

566   The strong TA flux to the overlying waters measured in the Rhône River delta, may contribute,

567 along with riverine inputs, to the overall high alkalinity of the Gulf of Lions waters compared to the

568 Mediterranean average (Cossarini et al., 2015). However, the influence of the benthic TA flux on the

569 water column pH and ultimately on the absorption of atmospheric CO_2 depends mainly on the TA to

570 DIC benthic flux ratio (F_{TA}/F_{DIC}), vertical mixing in the water column, and thus the residence time of

571 the bottom waters (Hu and Cai, 2011b, Andersson and Mackenzie, 2012). The F_{TA}/F_{DIC} ratios, ranging

572 between 0.8 and 1 in the proximal and prodelta zones of the Rhône River delta (Fig. 11), are in the

573 high range of a compilation of TA to DIC flux ratios obtained in different coastal systems and

574 continental shelves (expanded from Hu and Cai, 2011b). As these ratios do not exceed 1, alkalinity

575 generated in the sediments will not decrease pCO$_2$ in the bottom waters and thus not draw atmospheric

576 CO_2 into the coastal ocean. Yet, the large benthic TA fluxes generated from deltaic sediments and the

577 elevated F_{TA}/F_{DIC} (>0.8), which were unknown in the Rhône River prodelta before this study, may

578 modify the carbonate cycle paradigm in these coastal regions.

579 **5. Conclusion**

580   In this study, benthic respiration, as well as benthic alkalinity and DIC fluxes were quantified in

581 the Rhône River delta using benthic landers. These measurements demonstrated that sediments from

582 the proximal and prodelta domains represent a strong source of alkalinity to the water column. The

583 highest alkalinity and DIC fluxes were detected in the vicinity of the Rhône River mouth and were

584   much stronger than fluxes of dissolved oxygen, indicating the decoupling of oxic and anoxic

585   biogeochemical processes. As pore water oversaturation with respect to calcite prevented carbonate

586   dissolution to occur over the entire sediment column, the high benthic alkalinity fluxes resulted from

587   the high intensity of anaerobic respiration processes, mainly via sulfate reduction and precipitation

588   of iron sulfide minerals, but also with some contributions from dissimilatory iron reduction and AOM.

589   The intensity of sulfate reduction in the proximal domain also resulted in the consumption of a 10-

590   20% fraction of the alkalinity and DIC by the precipitation of authigenic carbonates. As the reduced

591   metabolites Fe^{2+} and $\sum H_2S$ produced by the mineralization of organic matter were buried in the solid

592   phase, alkalinity was not consumed by their reoxidation in the oxic sediment layers. Consequently, a

593   significant fraction of the total alkalinity generated in the pore waters was transferred to the bottom

594   waters (benthic flux of 14-74 mmol m^{-2} d^{-1}). Although sulfate reduction dominated the proximal and

595   prodelta domains, evidence for dissimilatory reduction of Fe(III) oxides was simultaneously observed

596   in the depth profiles, suggesting that anaerobic processes in the Rhône River prodelta are dynamic

597   and potentially controlled by pulsed sediment accumulations. The intensity of the alkalinity and DIC

598   fluxes decreased offshore as the sedimentation rate and the relative importance of anaerobic

599   mineralization pathways compared to aerobic processes decreased. In these conditions the more

600   "classical" coupling between aerobic and anaerobic reactions occurs, hence producing much lower

601   benthic alkalinity fluxes. Overall, these findings suggest that deltaic sediments exposed to large

602   riverine inputs of inorganic and organic material may provide a large source of alkalinity to the

603   overlying waters and thus weaken the increase in pCO$_2$ more significantly than previously thought in

604   coastal waters.

614 **References**

615   Aller, R. C., Blair, N. E., and Brunskill, G. J.: Early diagenetic cycling, incineration, and burial of
616   sedimentary organic carbon in the central Gulf of Papua (Papua New Guinea). J. Geophys. Res., 113:
617   1–22, 2008.

618   Aller, R. C., Mackin, J. E., and Cox, R. T.: Diagenesis of Fe and S in Amazon inner shelf muds:
619   apparent dominance of Fe reduction and implications for the genesis of ironstones. Cont. Shelf. Res.,
620   6: 263–289, 1986.

621   Andersson, A.J., Mackenzie, F.T. and Lerman, A: Coastal ocean CO_2-carbonic acid-carbonate
622   sediment system of the anthropocene. Glob. Biogochem. Cycle, 20, GB1S92, 2006.

623   Andersson, A. and Mackenzie, F.: Revisiting four scientific debates in ocean acidification research.
624   Biogeosci., 9: 893–905, 2012.

625   Anschutz, P., Zhong, S., Sundby, B., Mucci, A., and Gobeil, C.: Burial efficiency of phosphorus and
626   the geochemistry of iron in continental margin sediments. Limnol. Oceanogr., 43: 53–64, 1998.

627   Bauer, J. E., Cai, W.-J., Raymond, P. A., Bianchi, T. S., Hopkinson, C. S., and Regnier, P. A. G.: The
628   changing carbon cycle of the coastal ocean. Nature, 504(7478): 61–70, 2013.

629   Beckler, J., Nuzzio, D., and Taillefert, M.: Development of single-step liquid chromatography
630   methods with ultraviolet detection for the measurement of inorganic anions in marine waters. Limnol.
631   Oceanogr. Meth., 12: 563–576, 2014.

632   Beckler, J. S., Kiriazis, N., Rabouille, C., Stewart, F. J., and Taillefert, M.: Importance of microbial
633   iron reduction in deep sediments of river-dominated continental-margins. Mar. Chem., 178: 22–34,
634   2016.

635   Ben-Yaakov, S.: pH buffering of pore water of recent anoxic marine sediments. Limnol. Oceanogr.,
636   18(1): 86–94, 1973.

637   Berelson, W.M. et al.: Biogenic matter diagenesis on the sea floor: A comparison between two
638   continental margin transects. J. Mar. Res., 54: 731-762, 1996.

639   Berner, R. A.: Sedimentary pyrite formation. Am. J. Sci., 268: 1–23, 1970.

640 Berner, R. A.: Early Diagenesis: A Theoretical Approach. Princeton University Press, 1980.

641 Berner, R. A.: Burial of organic carbon and pyrite sulfur in the modern ocean; its geochemical and
642 environmental significance. Am. J. Sci., 282: 451–473, 1982.

643 Bianchi, S. T. and Allison, M. A.: Large-river delta-front estuaries as natural "recorders" of global
644 environmental change. Proc. Natl. Acad. Sci. U.S.A., 106: 8085–8092, 2009.

645 Borowski, W. S., Pau, C. K., and Ussler, W.: Marine pore-water sulfate profiles indicate in situ
646 methane flux from underlying gas hydrate. Geol., 24(7): 655–658, 1996.

647 Brenner, H., Braeckman, U., Le Guitton, M., and Meysman, F. J. R.: The impact of sedimentary
648 alkalinity release on the water column CO_2 system in the North Sea. Biogeosci., 13: 841–863, 2016.

649 Bristow, G. and Taillefert, M.: VOLTINT: A Matlab [R]-based program for semi-automated processing
650 of geochemical data acquired by voltammetry. Comp. Geosci., 29: 153–162, 2008.

651 Broecker, W. S. and Peng, T.-H.: Gas exchange rates between air and sea. Tellus, 26: 21–35, 1974.

652 Buffle, J.: Complexation reactions in aqueous systems: An Analytical Approach. Wiley and Sons,
653 1988.

654 Bura-Nakic, E., Viollier, E., Jezequel, D., Thiam, A., and Ciglenecki, I.: Reduced sulfur and iron
655 species in anoxic water column of meromictic crater Lake Pavin (Massif Central, France). Chem.
656 Geol., 266:311–317, 2009.

657 Burdige, D.J., Zimmerman, R.C.: Impact of sea grass density on carbonate dissolution in Bahamian
658 sediments. Limnol. Oceanogr., 47, 1751-1763, 2002.

659 Burdige, D.: Burial of terrestrial organic matter in marine sediments: A re-assessment. Glob.
660 Biogeochem. Cycles. 19. GB4011, doi:10.1029/2004/GB002368, 2005.

661 Burdige, D.: Estuarine and Coastal Sediments - Coupled Biogeochemical Cycling. Treat. Estuar.
662 Coast. Sci., 5: 279–316, 2011.

663 Burdige, D. J. and Komada, T.: Anaerobic oxidation of methane and the stoichiometry of
664 remineralization processes in continental margin sediments. Limnol. Oceanogr., 56(5): 1781–1796,
665 2011.

666 Cai, W.-J.: Estuarine and Coastal Ocean Carbon Paradox: CO_2 Sinks or Sites of Terrestrial Carbon
667 Incineration? Ann. Rev. Mar. Sci., 3(1): 123–145, 2011.

668 Cai, W.-J. and Reimers, C. E.: The development of pH and pCO_2 microelectrodes for studying the
669 carbonate chemistry of pore waters near the sediment-water interface. Limnol. Oceanogr., 38:1762–
670 1773, 1993.

671 Canfield, D. E., Jørgensen, B. B., Fossing, H., Glud, R., Gundersen, J., Ramsing, N. B., Thamdrup,
672 B., Hansen, J. W., Nielsen, L. P., and Hall, P.O.J.: Pathways of organic carbon oxidation in three
673 continental margin sediments. Mar. Geol., 113: 27–40, 1993a.

674 Canfield, D. E., Thamdrup, B., and Hansen, J. W.: The anaerobic degradation of organic matter in
675 Danish coastal sediments: iron reduction, manganese reduction, and sulfate reduction. Geochim.
676 Cosmochim. Acta, 57(16): 3867–3883, 1993b.

677 Carman, R. and Rahm, L.: Early diagenesis and chemical characteristics of interstitial water and
678 sediments in the deep deposition bottoms of the Baltic proper. J. Sci. Res., 37: 25–47, 1997.

679 Cathalot, C., Rabouille, C., Pastor, L., Deflandre, B., Viollier, E., Buscail, R., Grémare, A., Treignier,
680 C., and Pruski, A.: Temporal variability of carbon recycling in coastal sediments influenced by rivers:
681 assessing the impact of flood inputs in the Rhône River prodelta. Biogeosci., 7:1187–1205, 2010.

682 Cathalot, C., Rabouille, C., Tisnérat-Laborde, N., Toussaint, F., Kerhervé, P., Buscail, R., Loftis, K.,
683 Sun, M.-Y., Tronczynski, J., Azoury, S., Lansard, B., Treignier, C., Pastor, L., and Tesi, T.: The fate
684 of river organic carbon in coastal areas: A study in the Rhône River delta using multiple isotopic
685 ($\delta^{13}C$, $\Delta^{14}C$) and organic tracers. Geochim. Cosmichim. Acta, 118:33–55, 2013.

686 Charmasson, S., Radakovitch, O., Arnaud, M., Bouisset, P., and Pruchon, A.-S.: Long-core profiles
687 of ^{137}Cs, ^{134}Cs, ^{60}Co and ^{210}Pb in sediment near the Rhône River (Northwestern Mediterranean Sea).
688 Estuaries, 21(3):367–378, 1998.

689 Chen, C.-T. A. and Borges, A. V.: Reconciling opposing views on carbon cycling in the coastal ocean:
690 Continental shelves as sinks and near-shore ecosystems as sources of atmospheric CO_2 . Deep-Sea.
691 Res. II., 8: 578–590, 2009.

692 Clayton, T. D. and Byrne, R. H.: Spectrophotometric seawater pH measurements: total hydrogen ion
693 concentration scale calibration of m-cresol purple and at-sea results. Deep-Sea. Res. I., 40(10): 2115–
694 2129, 1993.

695 Cossarini, G., Lazzari, P., and Solidoro, C.: Spatiotemporal variability of alkalinity in the
696 Mediterranean Sea. Biogeosci., 12: 1647–1658, 2015.

697 Cyronak, T., Santos, I.R., McMahon, A., Eyre, B.D.: Carbon cycling hysteresis in permeable
698 carbonate sands over a diel cycle: Implications for ocean acidification. Limnol. Oceanogr., 58, 131-
699 143, 2013.

700 Davison, W., Buffle, J., and DeVitre, R.: Voltammetric characterization of a dissolved iron sulphide
701 species by laboratory and field studies. Anal. Chim. Acta, 377:193–203, 1998.

702 Davison, W.: The solubility of iron sulphides in synthetic and natural waters at ambient temperature.
703 Aquat. Sci., 53(4): 309-329, 1991.

704 Dickson, A. G.: An exact definition of total alkalinity and a procedure for the estimation of alkalinity
705 and total inorganic carbon from titration data. Deep-Sea. Res. A, 28 (6):609–623, 1981.

706 Dickson, A.G., Sabine, C.L., Christian, J.R.: Guide to best practices for ocean CO_2 measurements.
707 In: Dickson, A.G., Sabine, C.L., Christian, J.R. (Eds.), PICES Special Publication. 3. pp. 191, 2007.

708 Estournel, C., Kondrachoff, V., Marsaleix, P., and Vehil, R.: The Plume of the Rhone: numerical
709 simulation and remote sensing. Cont. Shelf. Res., 17(8):899–924, 1997.

710 Ferron, S., Alonso-Perez, F., Ortega, T. and Forja, J.M.: Benthic respiration on the northeastern shelf
711 of the Gulf of Cádiz. Mar. Ecol. Prog. Ser., 392: 69-80, 2009.

712 Friedl, G., Dinkel, C., and Wehrli, B.: Benthic fluxes of nutrients in the northwestern Black Sea. Mar.
713 Chem., 62:77–88, 1998.

714 Gaillard, J.-F., Pauwels, H., and Michard, G.: Chemical diagenesis in coastal marine sediments.
715 Oceanol. Acta, 12(3):173–187, 1989.

716 Got, H. and Aloisi, J. C.: The Holocene sedimentation on the Gulf of Lions margin: a quantitative
717 approach. Cont. Shelf. Res., 10(9-11):841–855, 1990.

718 Grasshof, K., Ehrhardt, M. and Kremling, K.: Methods of Seawater Analysis, second revised and
719 extended edition. Verlag Chemie GmbH, 420 pp, 1983.

720 Hammond, D.E., Giordani, P., Berelson, W.M. and Poletti, R.: Diagenesis of carbon and nutrients and
721 benthic exchange in sediments of the Northern Adriatic Sea. Mar. Chem., 66: 53-79, 1999.

722 Hartnett, H. E., Keil, R. G., Hedges, J. I., and Devol, A.: Influence of oxygen exposure time on organic
723 carbon preservation in continental margin sediments. Nature, 391:572–575, 1998.

724 Hedges, J. I. and Keil, R. G.: Sedimentary organic matter preservation: an assessment and speculative
725 synthesis. Mar. Chem., 49:81–115, 1995.

726 Henneke, E., Luther, G., and Delange, G.: Determination of inorganic Sulfur Speciation with
727 Polarographic Techniques - some preliminary Results for Recent Hypersaline Anoxic Sediments.
728 Mar. Geol., 100:115–123, 1991.

729 Hu, X. and Cai, W.-J.: An assessment of ocean margin anaerobic processes on oceanic alkalinity
730 budget. Glob. Biogeochem. Cycl., 25:1–11, 2011a.

731 Hu, X. and Cai, W.-J.: The impact of denitrification on the atmospheric CO_2 uptake potential of
732 seawater. Mar. Chem., 127: 192-198, 2011b.

733 Jahnke, R. A. and Christiansen, M. B.: A free-vehicle benthic chamber instrument for sea floor
734 studies. Deep-Sea. Res., 36(4): 625–637, 1989.

735 Jahnke, R. A.: A Global synthesis. In: Carbon and Nutrient Fluxes in Continental Margins, pages 597-
736 615. K.-K. Liu, L. Atkinson, R. Quinones, L. Talaue-McManus (eds), Berlin, 2010.

737 Jones, M., Fennessey, C., DiChristina, T., and Taillefert, M.: Shewanella oneidensis MR-1 mutants
738 selected for their inability to produce soluble organic-Fe(III) complexes are unable to respire Fe(III)
739 as anaerobic electron acceptor. Envir. Microb., 12: 938–950, 2010.

740 Jørgensen, B. B. and Kasten, S.: Sulfur cycling and methane oxidation. In Marine Geochemistry. pp
741 271-310. Schulz H.D. et al. (eds), Springer Verlag, 2006.

742   Jourabchi, P., Van Cappellen, P., and Regnier, P.: Quantitative interpretation of pH distributions in
743   aquatic sediments: A reaction-transport modeling approach. Amer. J. Sci., 305(9): 919–956, 2005.

744   Komada, T., Burdige, D. J., Li, H.-L., Magen, C., Chanton, J. P., and Cada, A. K.: Organic matter
745   cycling across the sulfate-methane transition zone of the Santa Barbara Basin, California Borderland.
746   Geochim. Cosmochim. Acta, 176: 259–278, 2016.

747   Krumins, V., Gehlen, M., Arndt, S., Van Cappellen, P., and Regnier, P.: Dissolved inorganic carbon
748   and alkalinity fluxes from coastal marine sediments: model estimates for different shelf environments
749   and sensitivity to global change. Biogeosci., 10(1): 371–398, 2013.

750   Lansard, B., Rabouille, C., Denis, L., and Grenz, C.: In situ oxygen uptake rates by coastal sediments
751   under the influence of the Rhône River (NW Mediterranean Sea). Cont. Shelf. Res., 28(12): 1501–
752   1510, 2008.

753   Lansard, B., Rabouille, C., Denis, L., and Grenz, C.: Benthic remineralization at the land–ocean
754   interface: A case study of the Rhône River (NW Mediterranean Sea). Estuar. Coast. Shelf Sci., 81(4):
755   544–554, 2009.

756   Lehrter, J., Beddick, D., Devereux, R., Yates, D., and Murrel, M.: Sediment-water fluxes of dissolved
757   inorganic carbon, O_2, nutrients, and N_2 from the hypoxic region of the Louisiana continental shelf.
758   Biogeochem., 109 (1-3): 233–252, 2012.

759   Li, Y.-H. and Gregory, S.: Diffusion of ions in sea water and in deep-sea sediments. Geochim.
760   Cosmochim. Acta, 38: 703–714, 1974.

761   Łukawska-Matuszewska, K. and Graca, B.: Pore water alkalinity below the permanent halocline in
762   the Gdańsk Deep (Baltic Sea) - Concentration variability and benthic fluxes. Mar. Chem., 204: 49-
763   61, 2018.

764   Luther, G. W. and Ferdelman, T.: Voltametric Characterization of Iron (II) Sulfide Complexes in
765   Laboratory Solutions and in Marine Waters and Porewaters. Environ. Sci. Technol., 27: 1154–1163,
766   1993.

767   Luther, G. W., Glazer, B., Ma, S., Trouwborst, R., Moore, T., Metzger, E., Kraiya, C., Waite, T.,
768   Druschel, G., Sundby, B., Taillefert, M., Nuzzio, D., Shank, T., Lewis, B., and Brendel, P.: Use of
769   voltammetric solid-state (micro)electrodes for studying biogeochemical processes: Laboratory
770   measurements to real time measurements with an in situ electrochemical analyzer(ISEA). Mar.
771   Chem., 108:221–235, 2008.

772   Maillet, G.M. Vella, C., Berné, S., Friend, P. L., Amos, C. L., Fleury, T. J. and Normand, A.: Mor-
773   phological changes and sedimentary processes induced by the December 2003 flood event at the
774   present mouth of the Grand Rhône River (southern France). Mar. Geol., 234(1): 159-177, 2006.

775   McKee, B. A., Aller, R. C., Allison, M. A., Bianchi, T. S., and Kineke, G. C.: Transport and
776   transformation of dissolved and particulate materials on continental margins influenced by major
777   rivers: benthic boundary layer and seabed processes. Cont. Shelf. Res., 24:899–926, 2004.

778 Millero, F.J. and Schreiber, D.R.: Use of the ion pairing model to estimate activity coefficients of the
779 ionic components of natural waters. Am. J. Sci., 282: 1508-1540, 1982.

780 Millero, F.J.: The estimation of the pK^{*}_{HA} of acids in seawater using the Pitzer equations. Geochim.
781 Cosmochim. Acta, 47: 2121-2129, 1983.

782 Millero, F. J.: Thermodynamics of the carbon dioxide system in the oceans. Geochim. Cosmochim.
783 Acta, 59, 661–677, 1995.

784 Miralles, J., Radakovitch, O., and Aloisi, J.-C.: ^{210}Pb sedimentation rates from the Nothwestern
785 Mediterranean margin. Mar. Geol., 216:155–167, 2005.

786 Mucci, A.: The solubility of calcite and aragonite in seawater at various salinities, temperatures and
787 one atmosphere total pressure, Am. J. Sci., 283, 780–799, 1983.

788 Mucci, A., Sundby, B., Gehlen, M., Arakaki, T., Zhong, S., and Silverberg, N.: The fate of carbon in
789 continental shelf sediments of eastern Canada: a case study. Deep S. Res. Part II: Topical Studies in
790 Oceanography, 47:733–760, 2000.

791 Muller-Karger, F.E. et al. : The importance of continental margins in the global carbon cycle,
792 Geophys. Res. Lett., 32, L01602, doi:10.1029/2004GL021346, 2005.

793 Murphy, J. and Riley, J. P.: A modified single solution method for determination of phosphate in
794 natural waters. Anal. Chim. Acta, 27:31–36, 1962.

795 Nakayama, N., Tokieda, T., Suzuki, A., Kim, T., Gamo, T., and Obata, H.: Size fractionation of
796 nanoparticulate metal sulfides in oxic water of Lake Teganuma, Japan. Geochem. J., 50:281–286,
797 2016.

798 Ortega, T., Ponce, R., Forja, J. and Gomez-Parra, A.: Benthic fluxes of dissolved inorganic carbon in
799 the Tinto-Odiel system (SW of Spain). Cont. Shelf. Res., 28: 458-469, 2008.

800 Pastor, L., Cathalot, C., Deflandre, B., Viollier, E., Soetaert, E., Meysmann, K., Ulses, F. J. R.,
801 Metzger, C., and Rabouille, C.: Modeling biogeochemical processes in sediments from the Rhône
802 River prodelta area (NW Mediterranean Sea). Biogeosci., 8:1351–1366, 2011.

803 Pyzik, A. and Sommer, S.: Sedimentary Iron Monosulfides - Kinetics and Mechanism of Formation.
804 Geochim. Cosmochim. Acta, 45:687–698, 1981.

805 Rabouille, C., Mackenzie, F. T. and Ver, L. M.: Influence of the human perturbation on carbon,
806 nitrogen, and oxygen biogeochemical cycles in the global coastal ocean. Geochim. Cosmochim. Acta
807 65: 3615-3641, 2001.

808 Rabouille, C., Denis, L., Dedieu, K., Stora, G., Lansard, B., and Grenz, C.: Oxygen demand in coastal
809 marine sediments: comparing in situ microelectrodes and laboratory core incubations. J. Exp. Mar.
810 Biol. Ecol., 285:49–69, 2003.

811 Radakovitch, O., Cherry, R., and Heussner, S.: ^{210}Pb and ^{210}Po: tracers of particle transfer on the
812 Rhône continental margin (NW Mediterranean). Deep S. Res. Part I: Oceanogr. Res. Pap.,
813 46(9):1539–1563, 1999.

814 Rao, A.M.F., Malkin, S.Y., Montserrat, F. and Meysman, F.J.R.: Alkalinity production in intertidal
815 sands intensified by lugworm bioirrigation. Estuar. Coast. shelf Sci., 148, 36-47, 2014.

816 Rassmann, J., Lansard, B., Pozzato, L., and Rabouille, C.: Carbonate chemistry in sediment pore
817 waters of the Rhône River delta driven by early diagenesis (NW Mediterranean). Biogeosci., 13(18):
818 5379–5394, 2016.

819 Rickard, D. and Luther, G. W.: Kinetics of pyrite formation by the H_2S oxidation of iron(II)
820 monosulfide in aqueous solutions between 25 and 125 °C: the mechanism. Geochem. Cosmochem.
821 Acta, 61:135–147, 1997.

822 Roussiez, V., Aloisi, J.-C., Monaco, A., and Ludwig, W.: Early muddy deposits along the Gulf of
823 Lions shoreline: A key for a better understanding of land-to-sea transfer of sediments and associated
824 pollutant fluxes. Mar. Geol., 222-223:345–358, 2005.

825 Rowe, G., Kaegi, M., Morse, J., Boland, G., and Briones, E.: Sediment community metabolism
826 associated with continental shelf hypoxia, Northern Gulf of Mexico. Estuaries, 25: 1097–1106, 2002.

827 Rozan, T., Taillefert, M., Trouwborst, R., Glazer, B., Ma, S., Herszage, J., Valdes, L., Price, K., and
828 Luther, G.: Iron-sulfur-phosphorus cycling in the sediments of a shallow coastal bay: Implications for
829 sediment nutrient release and benthic macroalgal blooms. Limnol. Oceanogr., 47: 1346–1354, 2002.

830 Sarradin, P.-M. and Caprais, J.-C.: Analysis of dissolved gases by headspace sampling gas
831 chromatography with column and detector switching. Preliminary results. Anal. Comm., 33:371–373,
832 1996.

833 Seeberg-Elverfeldt, J., Schlüter, M., Feseker, T., and Kölling, M.: Rhizon sampling of pore waters
834 near the sediment/water interface of aquatic systems. Limnol. Oceanogr. Meth., 3:361–371, 2005.

835 Sempéré, R., Charrière, B., Wambeke, F. V., and Cauwet, G.: Carbon inputs of the Rhône River to the
836 Mediterranean Sea: Biogeochemical implications. Glob. Biogeochem. Cycles, 14(2): 669–681, 2000.

837 Soetaert, K., Hofmann, A. F., Middelburg, J. J., Meysman, F. J. R., and Greenwood, J.: The effect of
838 biogeochemical processes on pH. Mar. Chem., 105: 30–51, 2007.

839 Stookey, L.: Ferrozine - a new spectrophotometric reagent for iron. Anal. Chem., 42(7): 779–781,
840 1970.

841 Taillefert, M., Beckler, J., Carey, E., Burns, J., Fennessey, C., and DiChristina, T.: Shewanella
842 putrefaciens produces an Fe(III)-solubilizing organic ligand during anaerobic respiration on insoluble
843 Fe(III) oxides. J. Inorg. Biochem. 101: 1760–1767, 2007.

844   Taillefert, M., Bono, A. B., and Luther, G. W.: Reactivity of freshly formed Fe(III) in synthetic
845   solutions and (pore)waters: Voltammetric evidence of an aging process. Environ. Sci. Technol.,
846   34(11):2169–2177, 2000.

847   Taillefert, M., Hover, V. C., Rozan, T. F., Theberge, S. M., and Luther, G. W.: The influence of sulfides
848   on soluble organic-Fe(III) in anoxic sediment porewaters. Estuaries, 25(6): 1088–1096, 2002.

849   Tercier-Waeber, M. and Taillefert, M.: Remote in situ voltammetric techniques to characterize the
850   biogeochemical cycling of trace metals in aquatic systems. J. Environ. Monitor., 10:30–54, 2008.

851   Theberge, S.M. and Luther III, G.W.: Determination of the electrochemical properties of a soluble
852   aqueous FeS species present in sulfidic solutions. Aquat. Geochem., 3: 191-211, 1997.

853   Thomas, H., Schiettecatte, L.-S., Suykens, K., Koné, Y. J. M., Shadwick, E. H., Prowe, A. E. F.,
854   Bozec, Y., de Baar, H. J., and Borges, A. V.: Enhanced ocean carbon storage from anaerobic alkalinity
855   generation in coastal sediments. Biogeosci., 6(2):267–274, 2009.

856   Wolf-Gladrow, D. A., Zeebe, R. E., Klaas, C., Körtzinger, A., and Dickson, A. G.: Total alkalinity:
857   The explicit conservative expression and its application to biogeochemical processes. Mar. Chem.,
858   106:287–300, 2007.

859

860 **Figure Captions**

861 **Figure 1:** Map of the Rhône River prodelta with the stations investigated during the AMOR-B-Flux

862 cruise in September 2015.

863

864 **Figure 2:** Dissolved oxygen and pH microprofiles recorded *in situ* at the sediment-water interface at

865 stations A, Z, K, and E. Stations A and Z are located in the proximal zone, K in the prodelta, and E in

866 the distal zone (i.e. continental shelf).

867

868 **Figure 3:** Temporal evolution of DIC and total alkalinity concentrations in the benthic chamber at

869 stations A, Z (measured during two deployments), and E. Error bars represent analytical uncertainties

870 determined from triplicate measurements. The benthic fluxes and their standard deviations are

871 provided in the text, in Figure 4 and in Table 2.

872

873 **Figure 4:** DIC and TA fluxes measured with the benthic chamber and diffusive oxygen uptake (DOU)

874 rates calculated from *in situ* microelectrode depth profiles at stations A, Z (measured during two

875 deployments), and E. Error bars represent either uncertainties about the linear regression of the

876 benthic DIC and TA gradients taking into account individual error bars of each data point or error

877 propagation and standard deviations of multiple DOU measurements. Fluxes out of the sediment are

878 positive and fluxes into the sediment are negative.

879

880 **Figure 5:** Depth profiles of dissolved O_2, Mn^{2+}, Fe^{2+}, org-Fe(III), FeS_{aq}, and ΣH_2S concentrations

881 measured electrochemically in intact sediment cores at stations A, Z, AK, K, B, and E. Org-Fe(III)

882 and FeS_{aq} are reported in normalized current intensities (nA).

883

884 **Figure 6:** Depth profiles of pore water TA, DIC, SO_4^{2-}, NH_4^+, CH_4, Ca^{2+}, nanoparticulate FeS (FeS_0),

885 ΣPO_4^{3-}, and AVS concentrations along with the calcium carbonate (calcite) saturation state of the pore

886   waters (Ω_{Ca}) at stations A, Z, AK, K, B, and E. Alternating symbol shapes indicate data collected from

887   duplicate long and short sediment cores. The calcium carbonate (calcite) saturation state (Ω_{Ca}) and

888   pore water FeS_0 concentrations were calculated whereas AVS was determined from solid phase

889   extractions. The two horizontal lines identify the sulfate-methane transition zone (SMTZ) found at

890   stations A and Z. Error bars represent standard deviations of multiple measurements for the

891   concentrations and error propagation for Ω. Concentrations of CH_4 were not measured at stations B,

892   K, and E.

893

894   **Figure 7:** Current intensities of organic-Fe(III) complexes as a function of Fe^{2+} concentrations

895   measured at each depth at stations A, Z, AK, B, and K compared to the same data obtained from iron-

896   rich deep-sea sediments (Beckler et al., 2016).

897

898   **Figure 8:** Calculated pIAP values as a function of depth into the sediment compared to the pK_{sp} of

899   amorphous FeS and mackinawite. Due to the lack of dissolved sulfide, the pIAP values in the pore

900   waters of station A and Z could not be calculated.

901

902   **Figure 9:** Average pore water saturation states with respect to calcite in the oxic sediment layers at

903   stations: a- Proximal (St. A, Z), b- prodelta (St. K), and c- distal (St. E) calculated using the DIC

904   gradients at the SWI together with the average measured pH microprofiles.

905

906   **Figure 10:** Conceptual model to visualize the link between the burial of iron sulfide minerals and

907   benthic alkalinity fluxes. The total alkalinity (TA) produced under anaerobic conditions at depth

908   diffuses upwards towards the aerobic sediment layer where it is consumed during reoxidation of Fe^{2+}

909   and $\Sigma H_2 S$ by dissolved oxygen (black). If the precipitation of sulfide minerals is significant, the

910   reduced iron and sulfide metabolites produced during anaerobic respiration are not reoxidized by

911 dissolved oxygen, and the TA produced is able to reach the bottom waters (red). The intensity of the

912 alkalinity flux into the bottom waters is indicated by the thickness of the arrow at the SWI.

913

914 **Figure 11:** TA to DIC benthic flux ratios as a function of depth at stations A, Z, and E of the Rhône

915 River delta compared to different coastal regions of water depth < 100 m where this ratio was

916 quantified from *in situ* benthic flux measurements (modified from Hu and Cai, 2011b). Other coastal

917 regions include Cadiz Bay and the Guadalquivir continental shelf (Spain; Ferron et al., 2009), the

918 Rio Tinto estuary (Spain; Ortega et al., 2008), the Po river delta and nearby Adriatic shelf (Italy;

919 Hammond et al. 1999), San Francisco Bay (USA; Hammond et al., 1985), and the California shelf

920 (USA; Berelson et al., 1996). The global coastal average TA to DIC flux ratio predicted from Krumins

921 et al., 2013 is also reported for reference. Note that this average is different from that reported by Hu

922 and Cai (2011b) which was corrected in their later publication (Hu and Cai, 2013).

923 **Table captions**

924 **Table 1:** Individual and consecutive microbial and abiotic reactions that affect the theoretical

925 $\Delta TA/\Delta DIC$ (r_{AD}), $\Delta DIC/\Delta SO_4$ (r_{DS}), and $\Delta TA/\Delta$sulfate (r_{AS}) stoichiometric ratios. Note that Eq. 14

926 and 17 include oxidation of H_2 produced by pyritization (Eq. 11) by sulfate-reducing bacteria.

927

928 **Table 2:** Sampling sites during the AMOR-B-Flux cruise in September 2015 and main characteristics

929 of bottom waters; dist. = distance to the Rhône River mouth; ω = sedimentation rate; Station Z was

930 sampled twice (Z on 09/08/15 and Z' on 09/14/15) to investigate temporal variability; n.d. = not

931 determined.

932

933 **Table 3:** Diffusion-corrected stoichiometric ratios corrected (r_{ADc} , r_{DSc}, and r_{ASc}) or not (r_{AD}, r_{DS}, and

934 r_{AS}) for carbonate precipitation along with their associated determination coefficients (r^2) from linear

935 regression coefficients.

936

937 **Table 4:** Calculated FeS burial fluxes and their TA-equivalent production at each station compared

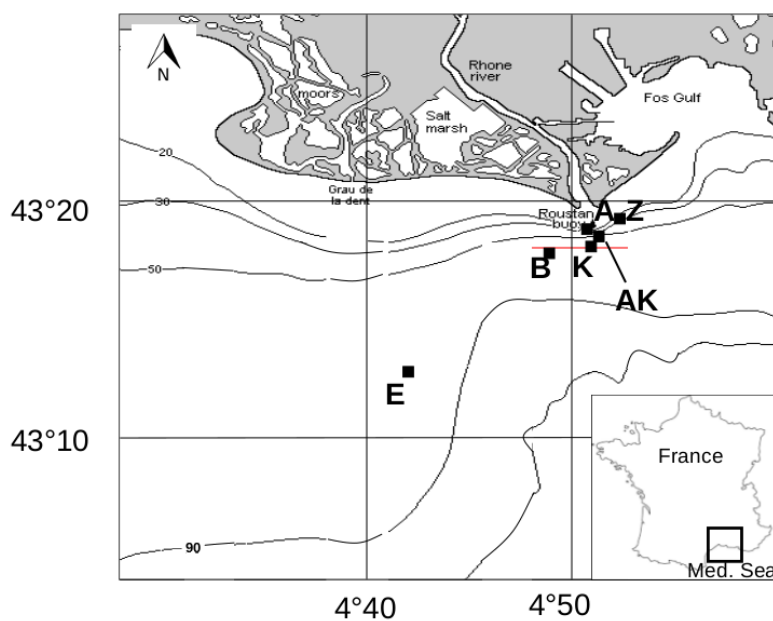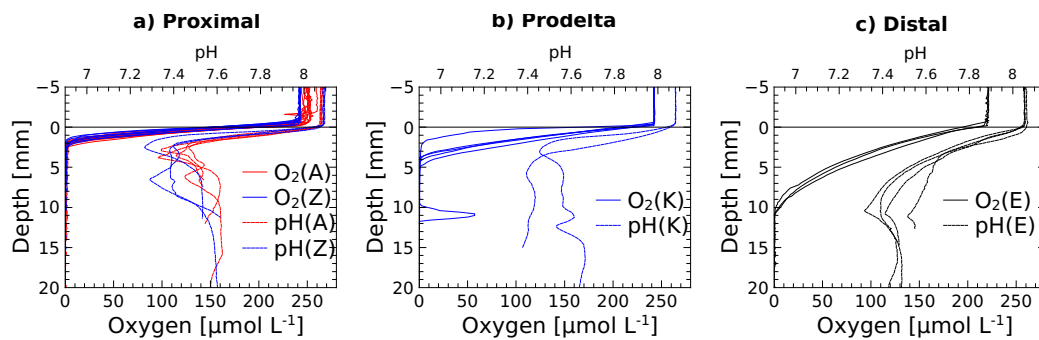938 to TA benthic fluxes measured; n.d. = not determined.
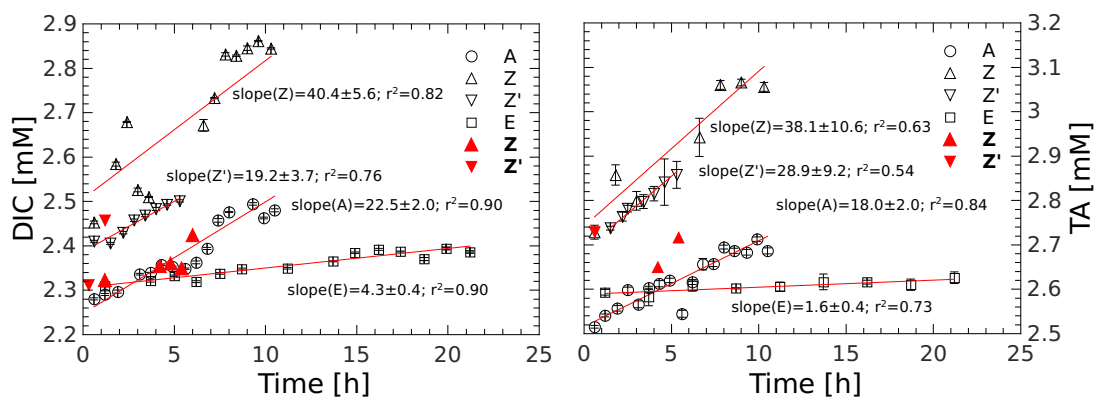
939

Figure 1: Figure 1

Figure 2: Figure 2

Figure 3: Figure 3
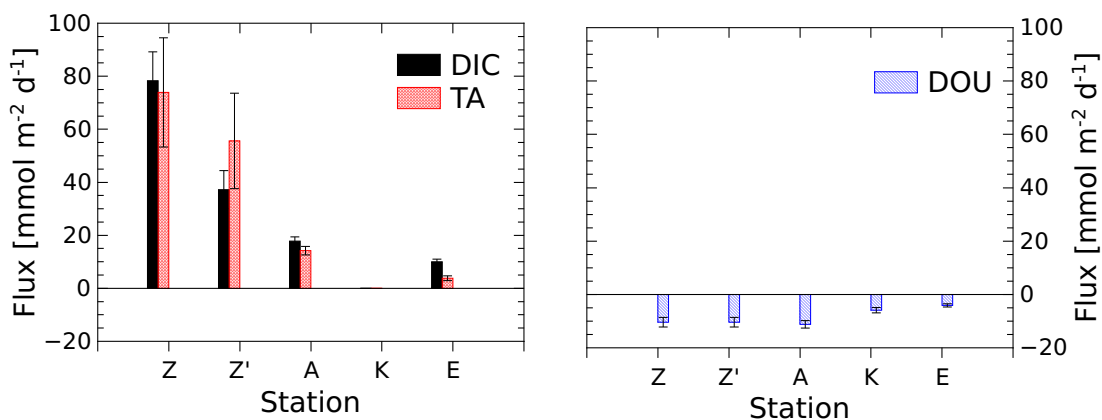
Figure 4: Figure 4
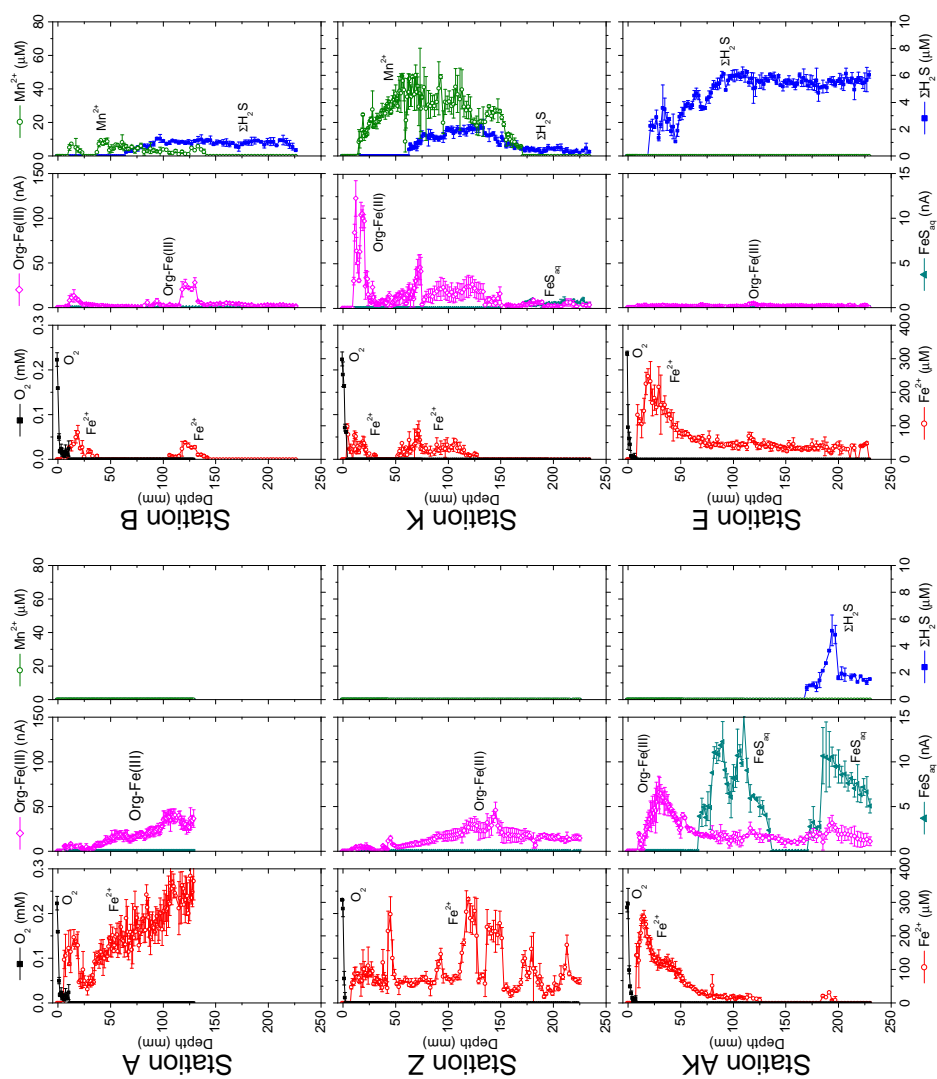
Figure 5: Figure 5
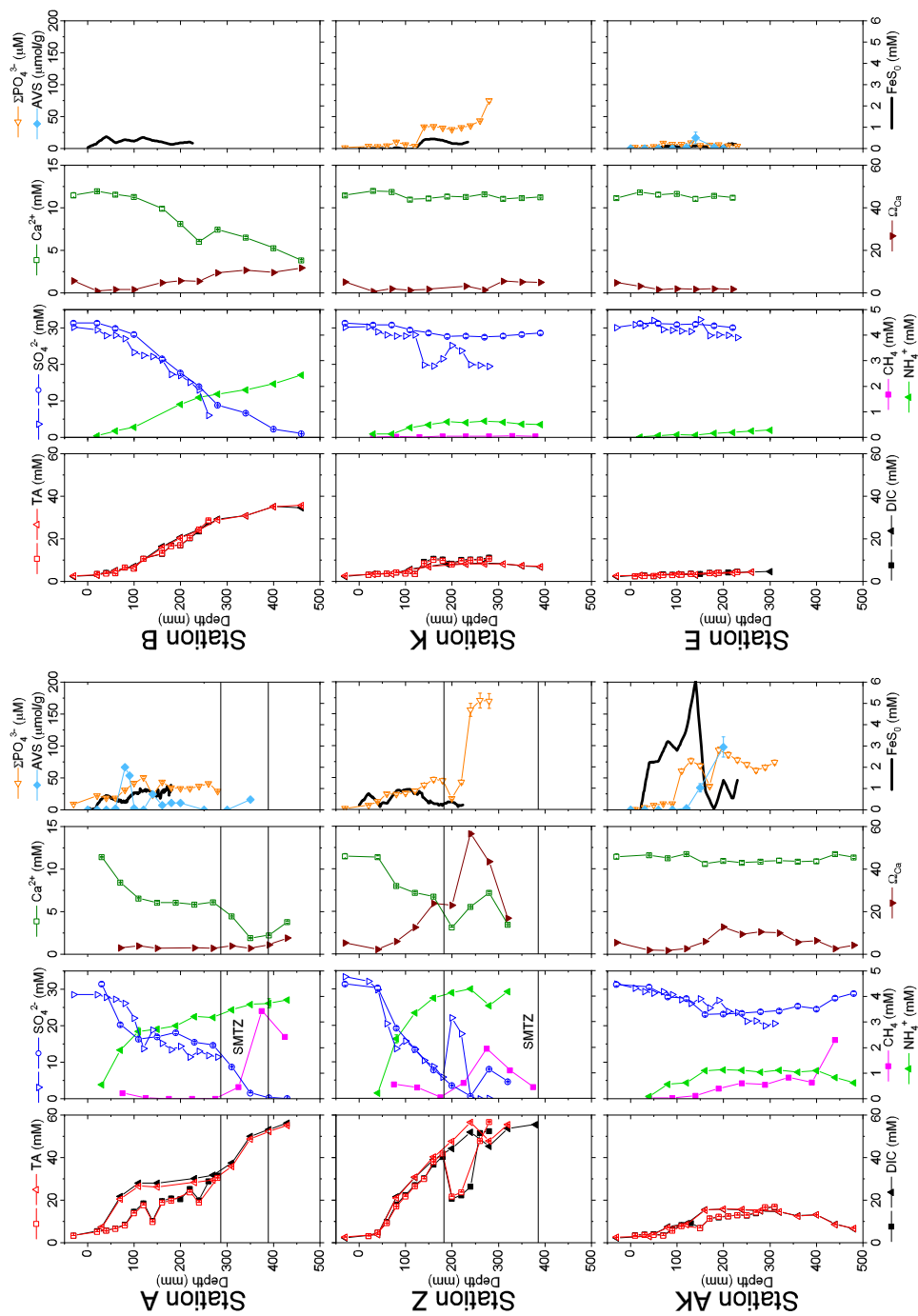
Figure 6: Figure6
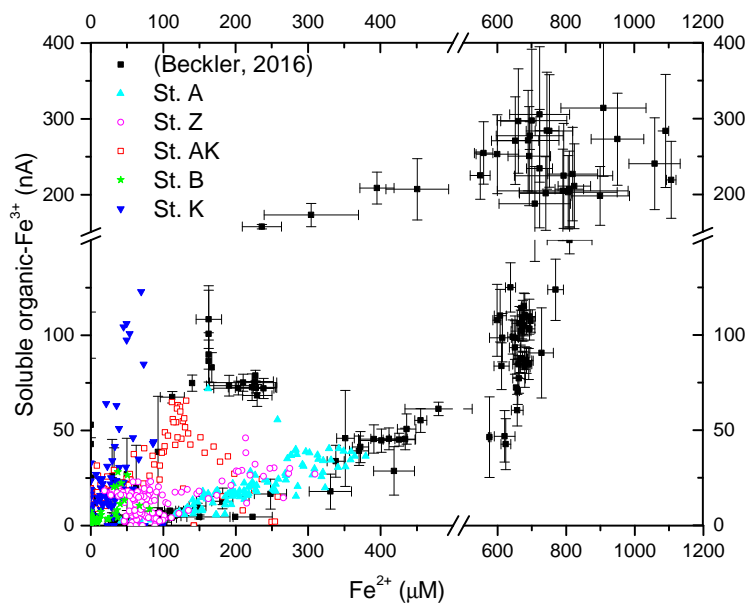
Figure 7: Figure 7
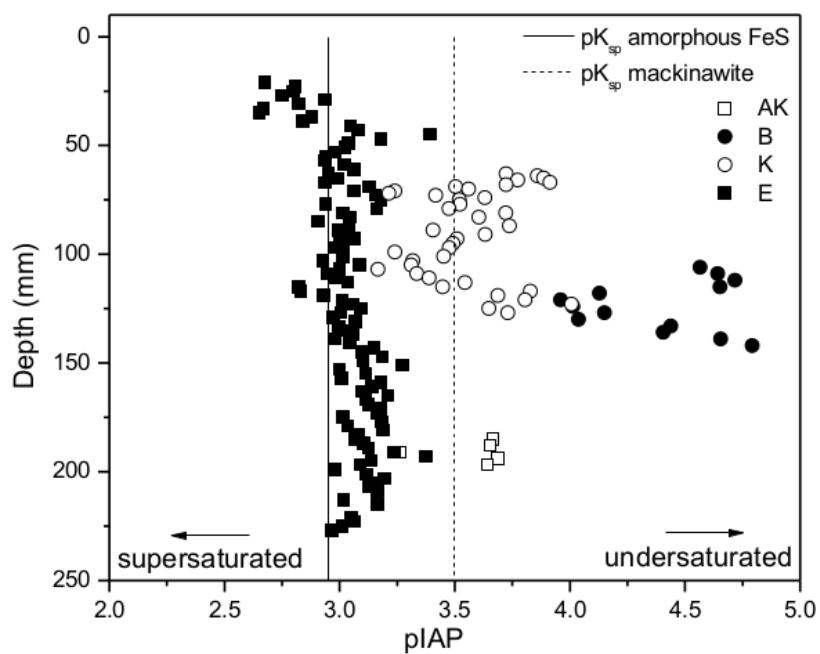
Figure 8: Figure 8
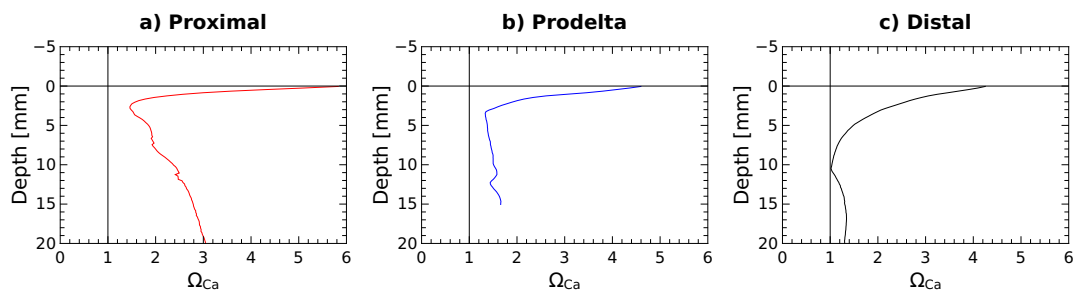
Figure 9: Figure 9

Figure 10: Figure 10

Figure 11: Figure 11

Biogeosciences Discussions — EGU Open Access

Table 1. Individual and consecutive microbial and abiotic reactions that affect the theoretical ΔTA/ΔDIC (r_{AD}), ΔDIC/Δsulfate (r_{DS}), and ΔTA/Δsulfate (r_{AS}) stoichiometric ratios. Note that Eq. 13 and 16 include oxidation of H$_2$ by sulfate reducing bacteria.

	Individual Reactions	r_{AD}	r_{DS}	r_{AS}
(1)	$Ca^{2+} + HCO_3^- \rightarrow CaCO_3 + H^+$	$\frac{-2}{-1}=2$	-	-
(2)	$NH_4^+ + 2O_2 \rightarrow NO_3^- + 2H^+ + H_2O$	$\frac{-2}{0}$	-	-
(3)	$Fe^{2+} + \frac{1}{4}O_2 + \frac{5}{2}H_2O \rightarrow Fe(OH)_3 + 2H^+$	$\frac{-2}{0}$	-	-
(4)	$H_2S + 2O_2 \rightarrow SO_4^{2-} + 2H^+$	$\frac{-2}{0}$	-	$\frac{-2}{+1}=-2$
(5)	$CH_2O + \frac{4}{5}NO_3^- - \frac{2}{5}H^+ \rightarrow HCO_3^- + \frac{2}{5}N_2 + \frac{2}{5}H_2O$	$\frac{+4/5}{+1}=0.8$	-	-
(6)	$2CH_2O + SO_4^{2-} \rightarrow 2HCO_3^- + H_2S$	$\frac{+2}{+2}=1$	$\frac{+2}{-1}=-2$	$\frac{+2}{-1}=-2$
(7)	$CH_2O + 4Fe(OH)_3 + 7H^+ \rightarrow HCO_3^- + 4Fe^{2+} + 10H_2O$	$\frac{+8}{+1}=8$	-	-
(8)	$CH_4 + SO_4^{2-} + H^+ \rightarrow HCO_3^- + H_2S + H_2O$	$\frac{+2}{+1}=2$	$\frac{+1}{-1}=-1$	$\frac{+2}{-1}=-2$
(9)	$Fe(OH)_{3(s)} + \frac{1}{2}H_2S + 2H^+ \rightarrow Fe^{2+} + \frac{1}{2}S(0) + 3H_2O$	$\frac{+2}{0}$	-	-
(10)	$Fe^{2+} + H_2S \rightarrow FeS_{(s)} + 2H^+$	$\frac{-2}{0}$	-	-
(11)	$FeS_{(s)} + H_2S \rightarrow FeS_{2(s)} + H_2$	$\frac{0}{0}$	-	-

	Consecutive Reactions	r_{AD}	r_{DS}	r_{AS}
	Sulfate reduction, abiotic reduction of Fe(III) oxides, and precipitation of sulfide minerals			
(12)	$2CH_2O + SO_4^{2-} + Fe(OH)_{3(s)} \rightarrow 2HCO_3^- + \frac{1}{3}S(0) + \frac{2}{3}FeS_{(s)} + 2H_2O$	$\frac{+2}{+2}=1$	$\frac{+2}{-1}=-2$	$\frac{+2}{-1}=-2$
(13)	$2CH_2O + SO_4^{2-} + \frac{2}{5}Fe(OH)_{3(s)} \rightarrow 2HCO_3^- + \frac{1}{5}S(0) + \frac{2}{5}FeS_{2(s)} + \frac{6}{5}H_2O + \frac{2}{5}H_2$	$\frac{+2}{+2}=1$	$\frac{+2}{-1}=-2$	$\frac{+2}{-1}=-2$
(14)	$\frac{20}{11}CH_2O + SO_4^{2-} + \frac{4}{11}Fe(OH)_{3(s)} + \frac{2}{11}H^+ \rightarrow \frac{20}{11}HCO_3^- + \frac{2}{11}S(0) + \frac{4}{11}FeS_{2(s)} + \frac{1}{11}H_2S + \frac{16}{11}H_2O$	$\frac{+2}{+\frac{20}{11}}=1.1$	$\frac{+\frac{20}{11}}{-1}=-1.8$	$\frac{+2}{-1}=-2$
	Concomitant dissimilatory iron and sulfate reduction with precipitation of sulfide minerals			
(15)	$\frac{9}{4}CH_2O + SO_4^{2-} + Fe(OH)_{3(s)} \rightarrow \frac{9}{4}HCO_3^- + \frac{1}{4}H^+ + FeS_{(s)} + \frac{5}{2}H_2O$	$\frac{+2}{+\frac{9}{4}}=0.89$	$\frac{+\frac{9}{4}}{-1}=-2.25$	$\frac{+2}{-1}=-2$
(16)	$\frac{17}{8}CH_2O + SO_4^{2-} + \frac{1}{2}Fe(OH)_{3(s)} \rightarrow \frac{17}{8}HCO_3^- + \frac{1}{8}H^+ + \frac{1}{2}FeS_{2(s)} + \frac{5}{4}H_2O + \frac{1}{2}H_2$	$\frac{+2}{+\frac{17}{8}}=0.94$	$\frac{+\frac{17}{8}}{-1}=-2.13$	$\frac{+2}{-1}=-2$
(17)	$\frac{17}{9}CH_2O + SO_4^{2-} + \frac{4}{9}Fe(OH)_{3(s)} + \frac{1}{9}H^+ \rightarrow \frac{17}{9}HCO_3^- + \frac{4}{9}FeS_{2(s)} + \frac{1}{9}H_2S + \frac{14}{9}H_2O$	$\frac{+2}{+\frac{17}{9}}=1.06$	$\frac{+\frac{17}{9}}{-1}=-1.89$	$\frac{+2}{-1}=-2$

Table 2. Sampling sites during the AMOR-B-Flux cruise in September 2015 and main characteristics of bottom waters; dist. = distance to the Rhône River mouth; ω = sedimentation rate; Station Z was sampled twice (Z on 09/08/15 and Z' on 09/14/15) to investigate temporal variability; n.d. = not determined.

Domain	Proximal			Prodelta			Distal
Stations	**A**	**Z**	**Z'**	**AK**	**B**	**K**	**E**
Long. ° E	4.850	4.868	4.868	4.853	4.833	4.858	4.684
Lat. °N	43.311	43.318	43.318	43.307	43.305	43.301	43.220
Dist. [km]	2.1	2.2	2.2	2.8	3	3.3	14.3
Depth [m]	20	20	20	42	50	58	72.5
Temp. [°C]	16.3	19.6	14.7	16.2	20.6	14.7	14.3
Salinity	37.5	37.6	37.7	37.7	38.0	37.7	37.8
O_2 [µM]	253.1 ± 0.3	249.5 ± 0.3	242.6 ± 0.2	250.2 ± 0.1	n.d.	241.8 ± 0.2	221.5 ± 0.3
DIC [mM]	2.29 ± 0.01	2.31 ± 0.01	n.d.	2.28 ± 0.01	2.27 ± 0.01	2.31 ± 0.01	2.33 ± 0.01
TA [mM]	2.61 ± 0.02	2.60 ± 0.01	n.d.	2.60 ± 0.02	2.60 ± 0.01	2.60 ± 0.02	2.61 ± 0.01
pH_T	8.08 ± 0.01	8.06 ± 0.01	8.09 ± 0.01	8.09 ± 0.01	8.07 ± 0.01	8.08 ± 0.01	8.05 ± 0.01
mean ϕ	0.69 ± 0.04	0.65 ± 0.04	0.65 ± 0.04	0.68 ± 0.02	0.66 ± 0.03	0.65 ± 0.05	0.64 ± 0.04
w [cm yr^{-1}]	30 - 40[a]			1 - 4[b]			0.1 - 1[c]
Benthic fluxes (mmol m^{-2} d^{-1})							
TA flux	14.3 ± 1.6	73.9 ± 20.6	56.0 ± 17.8	n.d.	n.d.	n.d.	3.7 ± 0.9
DIC flux	17.8 ± 1.6	78.3 ± 10.9	37.2 ± 7.2	n.d.	n.d.	n.d.	9.9 ± 0.9
DOU	10.2 ± 1.3	10.4 ± 0.9	n.d.	n.d.	n.d.	5.9 ± 1.0	3.6 ± 0.6

a. Data from Charmasson et al., 1998
b. Data from Lansard et al., 2009
c. Data from Miralles et al., 2005

Table 3. Diffusion-corrected stoichiometric ratios r_{AD}, r_{DS}, and r_{AS} and their corresponding ratios corrected for carbonate precipitation (r_{ADc}, r_{DSc}, and r_{ASc}) along with their associated determination coefficients (r^2) from linear regression; n.d = not determined.

Stations	A	Z	AK	B	K	E
r_{AD}	0.99 ± 0.01	1.08 ± 0.02	1.02 ± 0.02	1.02 ± 0.01	0.98 ± 0.05	0.90 ± 0.04
r^2	0.998	0.997	0.998	0.999	0.986	0.984
r_{ADc}	1.10 ± 0.01	1.16 ± 0.03	1.07 ± 0.02	1.15 ± 0.02	1.06 ± 0.07	1.15 ± 0.11
r^2	0.999	0.997	0.996	0.998	0.974	0.885
r_{DS}	-1.67 ± 0.06	-1.87 ± 0.17	-1.85 ± 0.05	-1.18 ± 0.05	-1.72 ± 0.03	n.d.
r^2	0.990	0.969	0.995	0.988	0.997	n.d.
r_{DSc}	-1.88 ± 0.05	-2.05 ± 0.18	-1.95 ± 0.05	-1.37 ± 0.05	-1.86 ± 0.07	n.d.
r^2	0.994	0.972	0.996	0.990	0.994	n.d.
r_{AS}	-1.66 ± 0.07	-2.03 ± 0.17	-1.89 ± 0.06	-1.21 ± 0.04	-1.69 ± 0.07	n.d.
r^2	0.986	0.973	0.992	0.994	0.991	n.d.
r_{ASc}	-2.07 ± 0.05	-2.35 ± 0.14	-2.01 ± 0.06	-1.58 ± 0.05	-1.89 ± 0.14	n.d.
r^2	0.994	0.977	0.989	0.992	0.958	n.d.

Table 4. Calculated FeS burial fluxes and their TA-equivalent production at each station compared to alkalinity fluxes measured; n.d. = not determined.

Stations	A and Z	AK	E
ω [cm yr^{-1}]	30	3	0.1
ϕ	0.67	0.68	0.64
Mean [AVS] [µmol g^{-1}]	19.5 ± 4.9	45.0 ± 11.3	9.0 ± 2.3
sediment density [g cm^{-3}]	2.5	2.5	2.5
FeS burial flux [mmol S m^{-2} d^{-1}]	12.5 ± 3.8	4.9 ± 1.4	0.02 ± 0.01
TA-equivalent prod. (=2.0 FeS) [mmol TA m^{-2} d^{-1}]	25 ± 8	9.8 ± 2.8	0.04 ± 0.1
Measured TA flux at SWI [mmol TA m^{-2} d^{-1}]	A : 14.3 ± 1.6 Z : 73.9 ± 20.6 Z' : 56.0 ± 17.8	n.d.	3.7 ± 0.9